

AD-A191 286

AFATL-TR-87-57

E801605

(2)

DTIC FILE COPY

Two- and Three-Dimensional Computational Analyses of Projectile-Concrete Impact

G R Johnson
R A Stryk

HONEYWEL, INC
ARMAMENT SYSTEMS DIVISION
7225 NORTHLAND DRIVE
BROOKLYN PARK, MINNESOTA 55428

DECEMBER 1987

DTIC
ELECTED
JAN 20 1988
S D
H

FINAL REPORT FOR PERIOD SEPTEMBER 1983-JULY 1987

APPROVED FOR PUBLIC RELEASE; DISTRIBUTION UNLIMITED

AIR FORCE ARMAMENT LABORATORY
Air Force Systems Command ■ United States Air Force ■ Eglin Air Force Base, Florida

88 1 12 162

NOTICE

When Government drawings, specifications, or other data are used for any purpose other than in connection with a definitely Government-related procurement, the United States Government incurs no responsibility nor any obligation whatsoever. The fact that the Government may have formulated or in any way supplied the said drawings, specifications, or other data, is not to be regarded by implication or otherwise in any manner construed, as licensing the holder, or any other person or corporation; or as conveying any rights or permission to manufacture, use, or sell any patented invention that may in any way be related thereto.

The Public Affairs Office has reviewed this report, and it is releasable to the National Technical Information Service (NTIS), where it will be available to the general public, including foreign nationals.

This technical report has been reviewed and is approved for publication.

FOR THE COMMANDER



JOHN A. PALMER, Col., USAF
Chief, Munitions Division

Even though this report may contain special release rights held by the controlling office, please do not request copies from the Air Force Armament Laboratory. If you qualify as a recipient, release approval will be obtained from the originating activity by DTIC. Address your request for additional copies to:

Defense Technical Information Center
Cameron Station
Alexandria, VA 22304-6145

If your address has changed, if you wish to be removed from our mailing list, or if your organization no longer employs the addressee, please notify AFATL/MNW, Eglin AFB FL 32542-5434, to help us maintain a current mailing list.

Copies of this report should not be returned unless return is required by security considerations, contractual obligations, or notice on a specific document.

UNCLASSIFIED

SECURITY CLASSIFICATION OF THIS PAGE

AD-A191286

Form Approved
OMB No. 0704-0188

REPORT DOCUMENTATION PAGE

1a. REPORT SECURITY CLASSIFICATION Unclassified		1b. RESTRICTIVE MARKINGS										
2a. SECURITY CLASSIFICATION AUTHORITY		3. DISTRIBUTION/AVAILABILITY OF REPORT Approved for public release; distribution is unlimited.										
2b. DECLASSIFICATION/DOWNGRADING SCHEDULE												
4. PERFORMING ORGANIZATION REPORT NUMBER(S) 7-87-15		5. MONITORING ORGANIZATION REPORT NUMBER(S) AFATL-TR-87-57										
6a. NAME OF PERFORMING ORGANIZATION Honeywell	6b. OFFICE SYMBOL (if applicable)	7a. NAME OF MONITORING ORGANIZATION Clusters and Warheads Branch Munitions Division										
6c. ADDRESS (City, State, and ZIP Code) Honeywell Inc., Armament Systems Division 7225 Northland Drive Brooklyn Park, MN 55428		7b. ADDRESS (City, State, and ZIP Code) Air Force Armament Laboratory Eglin AFB, FL 32542-5434										
8a. NAME OF FUNDING/SPONSORING ORGANIZATION Munitions Division	8b. OFFICE SYMBOL (if applicable) AFATL/MNW	9. PROCUREMENT INSTRUMENT IDENTIFICATION NUMBER F08635-83-C-0506										
8c. ADDRESS (City, State, and ZIP Code) Air Force Armament Laboratory Eglin AFB, FL 32542-5434		10. SOURCE OF FUNDING NUMBERS PROGRAM ELEMENT NO. 62602F PROJECT NO. 2502 TASK NO. 07 WORK UNIT ACCESSION NO. 04										
11. TITLE (Include Security Classification) Two- and Three-Dimensional Computational Analysis of Projectile-Concrete Impact												
12 PERSONAL AUTHOR(S) G.R. Johnson, R.A. Stryk												
13a. TYPE OF REPORT Final	13b. TIME COVERED FROM Sep 83 TO Jul 87	14. DATE OF REPORT (Year, Month, Day) December 1987	15. PAGE COUNT 55									
16. SUPPLEMENTARY NOTATION Availability of this report is specified on verso of front cover.												
17. COSATI CODES <table border="1"><tr><th>FIELD</th><th>GROUP</th><th>SUB-GROUP</th></tr><tr><td>12</td><td>05</td><td></td></tr><tr><td>19</td><td>02</td><td></td></tr></table>		FIELD	GROUP	SUB-GROUP	12	05		19	02		18. SUBJECT TERMS (Continue on reverse if necessary and identify by block number) Concrete Impact, EPIC Hydrocodes Numerical Analysis	
FIELD	GROUP	SUB-GROUP										
12	05											
19	02											
19 ABSTRACT (Continue on reverse if necessary and identify by block number) This report examines various computational approaches for projectile impact onto concrete targets. Included are two- and three-dimensional computations performed with both the EPIC-2 and EPIC-3 codes. Various techniques, such as tunneling, eroding, and NABOR nodes, are used to compare results and demonstrate capabilities. Results are presented for normal, oblique, and yawed impact.												
This report also documents the NABOR algorithms for axisymmetric and three-dimensional geometry. These NABOR algorithms allow for variable nodal connectivity and are well suited for projectile-concrete impact problems.												
20 DISTRIBUTION/AVAILABILITY OF ABSTRACT <input type="checkbox"/> UNCLASSIFIED/UNLIMITED <input checked="" type="checkbox"/> SAME AS RPT. <input type="checkbox"/> DTIC USERS		21. ABSTRACT SECURITY CLASSIFICATION Unclassified										
22a. NAME OF RESPONSIBLE INDIVIDUAL MICHAEL E. NIXON		22b. TELEPHONE (Include Area Code) (904) 882-2145	22c. OFFICE SYMBOL AFATL/MNW									

PREFACE

This report was prepared by Honeywell Inc., Armament Systems Division, 7225 Northland Drive, Brooklyn Park, Minnesota 55428, for the U.S. Air Force Armament Laboratory (AFATL), Eglin Air Force Base, Florida 32542, Under Contract F08635-83-C-0506.

This effort was conducted from September 1983 to July 1987. The authors would like to thank Lts. Paul L. Thee and Dennis L. May, AFATL/MNW program managers, and William H. Cook and Michael E. Nixon, AFATL/MNW, for many helpful technical discussions. Jack G. Dodd, professor at Colgate University and consultant to Honeywell, also contributed to this work.

This report documents only the portion of the contract work concerned with projectile-concrete impact. This contract was also responsible for the development of the 1986 version of the EPIC-2 Code (Reference 1) and the 1987 version of the EPIC-3 Code (Reference 2).



Accession For	
NTIS	CRA&I <input checked="" type="checkbox"/>
DTIC TAB	<input type="checkbox"/>
Unannounced	<input type="checkbox"/>
Justification	

By	Distribution
Availability	Available
Dist	Special

R-1

TABLE OF CONTENTS

Section	Title	Page
I	INTRODUCTION	1
II	COMPUTATIONAL STUDY.....	2
	1. Two-Dimensional Computations	2
	2. Three-Dimensional Computations	12
III	NABOR ALGORITHMS.....	27
	1. Axisymmetric Geometry	27
	a. Strains and Strain Rates.....	27
	b. Deviator and Shear Stresses.....	31
	c. Pressure and Artificial Viscosity	34
	d. Concentrated Forces.....	35
	e. Equations of Motion	37
	f. Searching Algorithm	37
	2. Three-Dimensional Geometry	41
IV	CONCLUSIONS AND RECOMMENDATIONS.....	46
	REFERENCES	47

LIST OF FIGURES

Figure	Title	Page
1	Definition of Projectile Geometry.....	3
2	EPIC-2 Computation with Tunneling in Target.....	4
3	EPIC-2 Computation with Erosion in Target	5
4	EPIC-2 Computation with NABOR Nodes in Target.....	7
5	EPIC-2 Computation with Coarse Grid and Erosion in Target.....	8
6	Time Histories of Projectile Penetration Depth and Velocity for the EPIC-2 Computations	9
7	Time Histories of Equivalent Stress in the Projectile Case for the EPIC-2 Computations	10
8	Time Histories of Pressure in the Projectile Explosive for the EPIC-2 Computations	11
9	Time Histories of Axial Acceleration at the Aft End of the Projectile for the EPIC-2 Computations	13
10	View of the Three-Dimensional, EPIC-3 Grid.....	14
11	EPIC-3 Computation for Normal Impact, with Erosion in Target	15
12	EPIC-3 Computation for Normal Impact, with NABOR Nodes in Target	17
13	Time Histories of Projectile Penetration Depth and Velocity for EPIC-2 and EPIC-3 Computations	18
14	Time Histories of Equivalent Stress in the Projectile Case for the EPIC-3, Normal Impact Computations	19
15	Time Histories of Pressure in the Projectile Explosive for the EPIC-3, Normal Impact Computations	20
16	Time Histories of Axial and Transverse Acceleration at the Aft End of the Projectile for the EPIC-3, Normal Impact Computations	22
17	EPIC-3 Computation for Oblique Impact (30 Degrees from Normal) with Erosion in Target	23
18	EPIC-3 Computation for Yawed Impact (5 Degrees) with Erosion in Target	24
19	Time Histories of Equivalent Stress in the Projectile Case for the EPIC-3, Oblique and Yawed Impact Computations	25

LIST OF FIGURES (CONCLUDED)

Figure	Title	Page
20	Time Histories of Pressure in the Projectile Explosive for the EPIC-3, Oblique and Yawed Impact Computations	26
21	Schematic Representation of the NABOR Computational Technique in Plane Strain Geometry	28
22	Definition of Velocities and Strain Rates for Axisymmetric Geometry	29
23	Volumetric Strains for One-Dimensional Compression	32
24	Plastic Flow Relationships for Various Strain Rates	33
25	Definition of Nodal Forces for Axisymmetric Geometry	36
26	Derivation of Force-Stress Relationship for Hexagonal Nodal Arrangement in Axisymmetric Geometry	38
27	Schematic Representation of the Searching Algorithm	39
28	Arrangement of Three-Dimensional NABOR Nodes	42
29	Attachment of Three-Dimensional NABOR Nodes to Traditional Tetrahedral Element Grid	43

SECTION I

INTRODUCTION

When a steel projectile impacts a concrete target, some special computational capabilities are required. Generally, the projectile will undergo only mild deformations and its response is best represented by a Lagrangian code. The concrete target often experiences severe deformations, which can present problems for a Lagrangian code.

It is possible to predetermine a sliding interface at the axis of symmetry for normal impact of a pointed projectile. This approach was used by Thigpen (Reference 3), who used the Lagrangian TOODY code to compute the response of a projectile into rock targets.

If the projectile is not pointed, then it may not be possible to accurately predetermine the sliding interfaces in the same manner. An alternate approach, used by Osborn and Matuska (Reference 4), is to perform the computation in two phases. The first phase uses a rigid projectile and an Eulerian target, and the second phase uses a Lagrangian projectile with stresses applied at the boundary. These applied stresses are taken from the first phase of the computation and vary with position and time. The computations by Osborn and Matuska were performed with the Eulerian HULL code and the Lagrangian TOODY code.

Only a limited number of three-dimensional computations have been performed to date. Kimsey, Jonas, Zukas and Johnson (Reference 5) used the EPIC-3 code to determine ricochet conditions for a projectile impacting a concrete target. In these computations, the concrete target material was allowed to erode, such that it was not necessary to predetermine the sliding interfaces. This technique will be described in more detail later.

More recently, Rosinsky (Reference 6) used the DYNA3D code to perform three-dimensional, oblique impact computations for a pointed projectile. For these computations, it was necessary to predetermine the penetration path by inserting a small hole in the target. Because the path cannot generally be accurately predicted at the beginning of the computation, it is usually necessary to perform an iterated series of computations when using this approach.

This report presents two- and three-dimensional computations performed with the EPIC-2 and EPIC-3 codes. An eroding target approach is considered, as well as a NABOR node approach that uses variable connectivity. It begins by evaluating the approaches in two-dimensional, axisymmetric geometry, and then demonstrates them in three dimensions. Descriptions of the axisymmetric and three-dimensional NABOR algorithms are also included.

SECTION II COMPUTATIONAL STUDY

This section presents a series of two- and three-dimensional computations performed with the EPIC-2 and EPIC-3 codes (References 1 and 2). Figure 1 shows details of the projectile used for these computations.

The two-dimensional EPIC-2 grid uses triangular elements in a crossed triangle (four triangles per quadrilateral) arrangement. The three-dimensional EPIC-3 grid is composed of tetrahedral elements and is similar to the two-dimensional grid. In both instances, sliding is allowed to occur between the 4340 steel case and the inert explosive. It is assumed that there is no friction at the steel-explosive interface or at the steel-concrete interface.

The strength model for the 4340 steel was developed by Johnson and Cook (Reference 7), and the concrete model was developed by Matuska, Durrett and Osborn (Reference 8). For the computations in this paper, the density of the concrete is 2308 kg/m^3 , and the unconfined compressive strength is 34 megapascal (MPa). The inert explosive has a density of 1817 kg/m^3 and a yield stress of 14 MPa.

1. TWO-DIMENSIONAL COMPUTATIONS

Figure 2 shows an axisymmetric, tunneling computation, where the centerline nodes in the concrete target are designated as slave nodes, and the outer surface of the steel projectile is designated as the master surface. Due to the axisymmetric nature of this problem, it is possible to predetermine the path of the projectile, and this allows for the proper predetermination of the sliding interfaces. From a computational viewpoint, this problem is well defined, and it will be the baseline to which the other computations will be compared.

Figure 3 shows an axisymmetric, eroding computation, where all of the nodes in the center portion of the target are designated as slave nodes. Furthermore, the elements in the target are allowed to erode (or totally fail) when the equivalent plastic strain exceeds 1.5. When an element is eroded, it cannot develop any stresses or pressures. It essentially disappears, except that the mass is retained at the nodes.

Even though this erosion approximation may appear to be very severe, the depth of penetration for this computation is only 11 percent greater than for the tunneling (baseline) computation. Additional comparisons will be made later.

A distinct advantage of the erosion computation is that it requires significantly less Central Processor Unit (CPU) time. The erosion computation in Figure 3 required only 18 percent of the CPU time used for the tunneling computation of Figure 2. The reason for this large difference is that the center line target elements in the tunneling computation become very small in cross section as they move radially outward along the outside of the case. The small cross section leads to a small minimum altitude, which in turn leads to a small integration time increment. The net result is that the tunneling computation requires many more integration cycles.

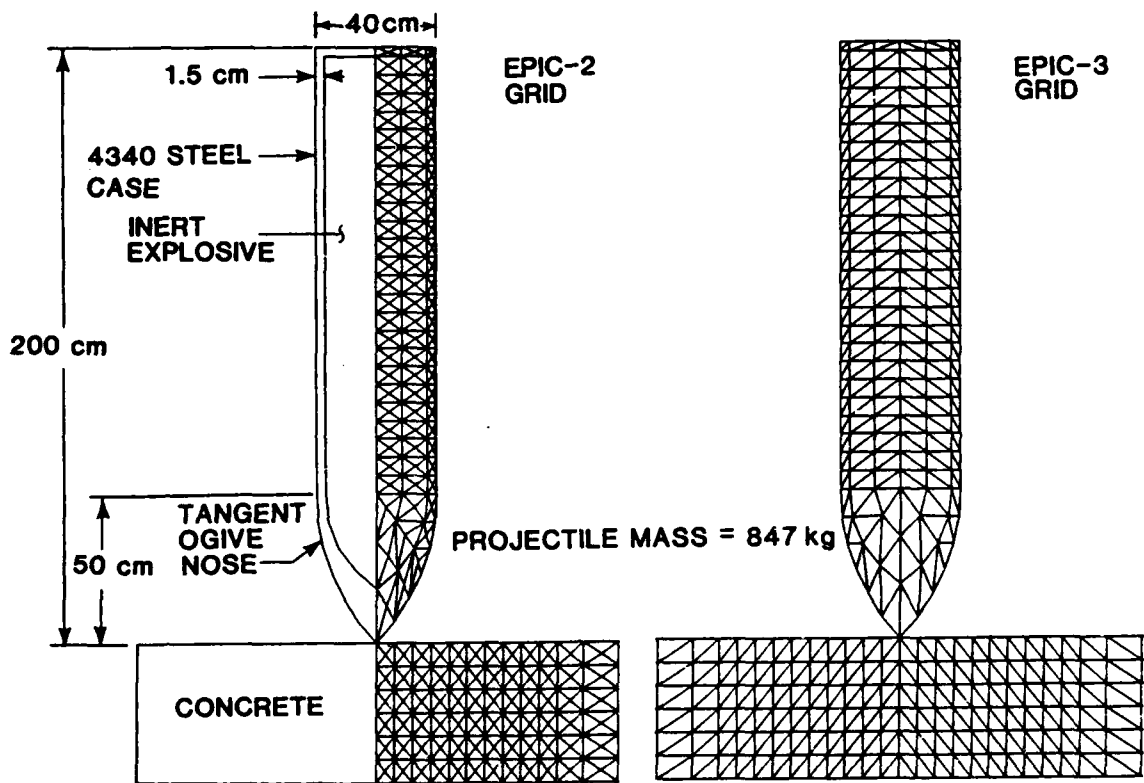


Figure 1. Definition of Projectile Geometry

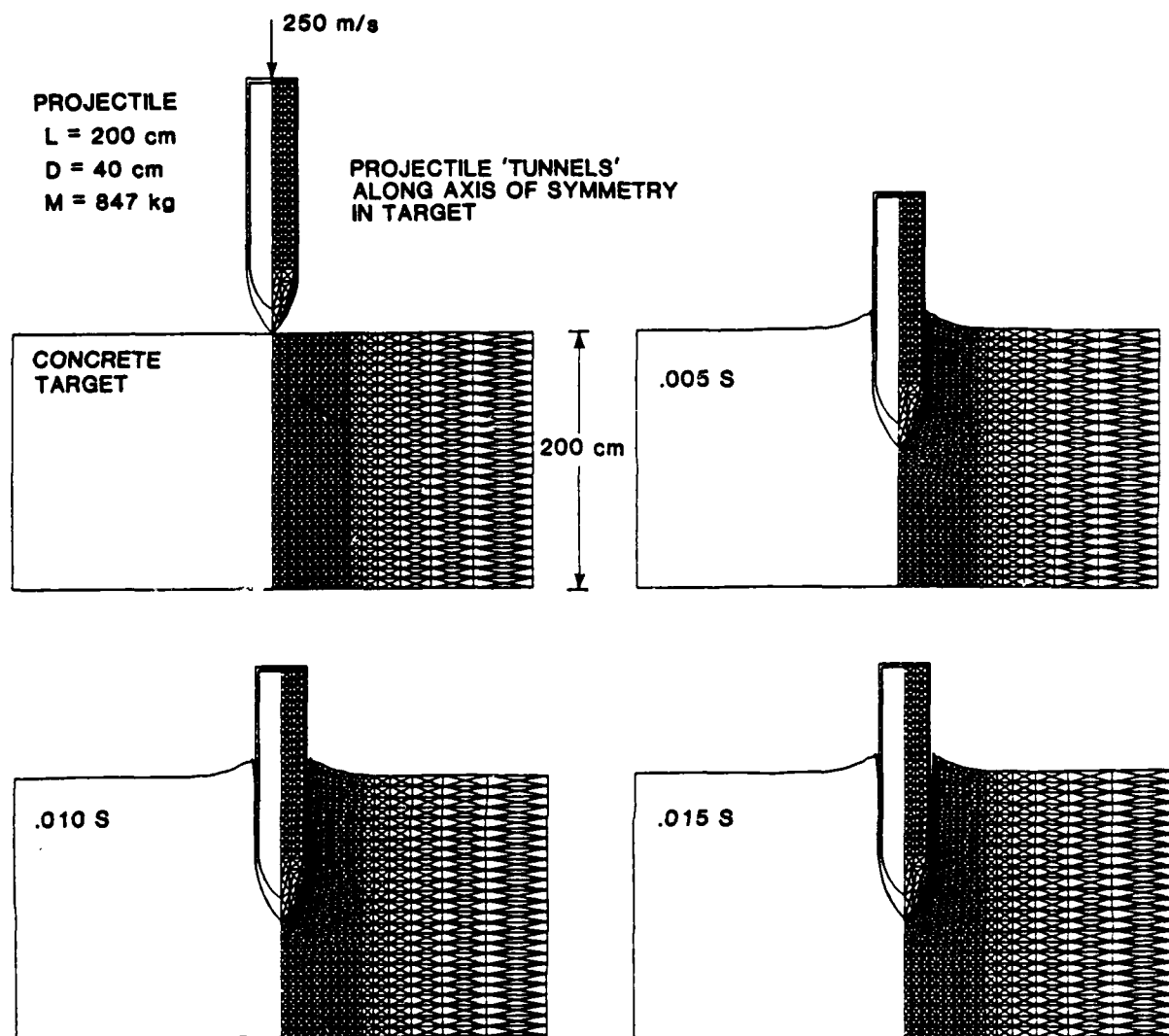


Figure 2. EPIC-2 Computation with Tunneling in Target

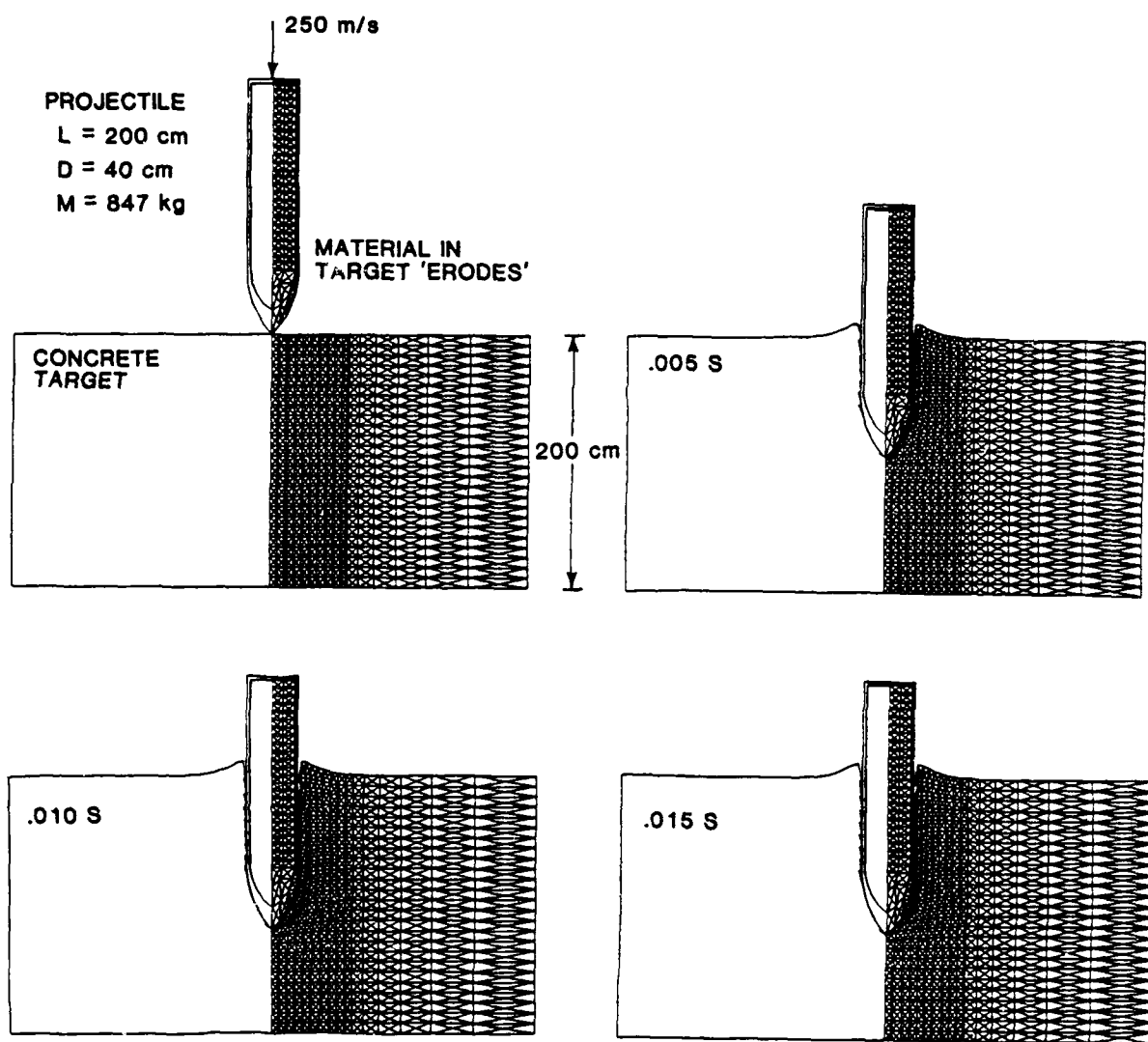


Figure 3. EPIC-2 Computation with Erosion in Target

The reason the time increment remains much larger for the erosion computation is that the center line elements are eroded when they become highly strained, and the eroded elements cannot govern the integration time increment. This leaves lower-strained elements, with larger altitudes, to govern the time increment.

Another distinct advantage of the eroding target approach is that it is not necessary to predetermine the path of the projectile or to predetermine the precise sliding interfaces. This is especially important in three dimensions. All of the nodes in the appropriate portion of the target are designated as slave nodes, and the projectile simply follows the path of the least resistance, as governed by the mechanics in the numerical algorithm.

Figure 4 shows an axisymmetric NABOR computation, where the nodes in the center portion of the target are designated as NABOR nodes. They are also designated as slave nodes. The NABOR option allows for variable nodal connectivity. Each node is affected only by its nearest neighbor nodes. As the nodes move closer than their equilibrium distance, they generate compressive, repulsive forces. Conversely, when they move apart they can generate tensile attractive forces. Material strength effects are also included. The key to this approach is that it is possible to have variable nodal connectivity. A node can take on new nearest neighbors thus allowing all forms of distortion. Based on the concept of nearest neighbors, this option has been designated the NABOR option. The specific algorithm will be presented in the next section.

The NABOR results shown in Figure 4 are in good general agreement with the previous computations, with the depth of penetration being 14 percent greater than the depth obtained from the tunneling (baseline) computation.

Some other features of this approach should also be noted. Because it is a Lagrangian algorithm (the mass moves with the grid), it is possible to connect the NABOR nodes to the traditional finite element grid as shown in Figure 4. It is also possible to designate the NABOR nodes as slave nodes such that they can slide along the master surface on the projectile. Like the eroding target approach discussed previously, there is no need to predetermine the penetration path or the precise sliding interface. The path is automatically determined from the mechanics in the numerical algorithm.

Although the results of the eroding computation in Figure 3 appear to be similar to the results of the NABOR computation in Figure 4, the two methods may not be similar for all cases. The eroding target approach may not be as accurate as the NABOR approach for blunt nose shapes. Conversely, the NABOR approach incorporates many simplifying assumptions and its accuracy has not been verified for a wide range of problems. Nevertheless, the initial results with both approaches are very encouraging.

Another factor that should be considered when performing comparative computations is the effect of the grid size. Figure 5 shows the results of a coarser grid in the target when using the eroding target approach. Here, the number of target elements is only half as many as used in the computations of Figures 2 and 3. When compared to the eroding target computation of Figure 3, the coarser grid computation of Figure 5 produces a maximum penetration depth which is only 3 percent less.

Figure 6 shows penetration depth and velocity for the four computations shown in Figures 2 through 5. The tunneling (baseline) computation is probably the most accurate but the

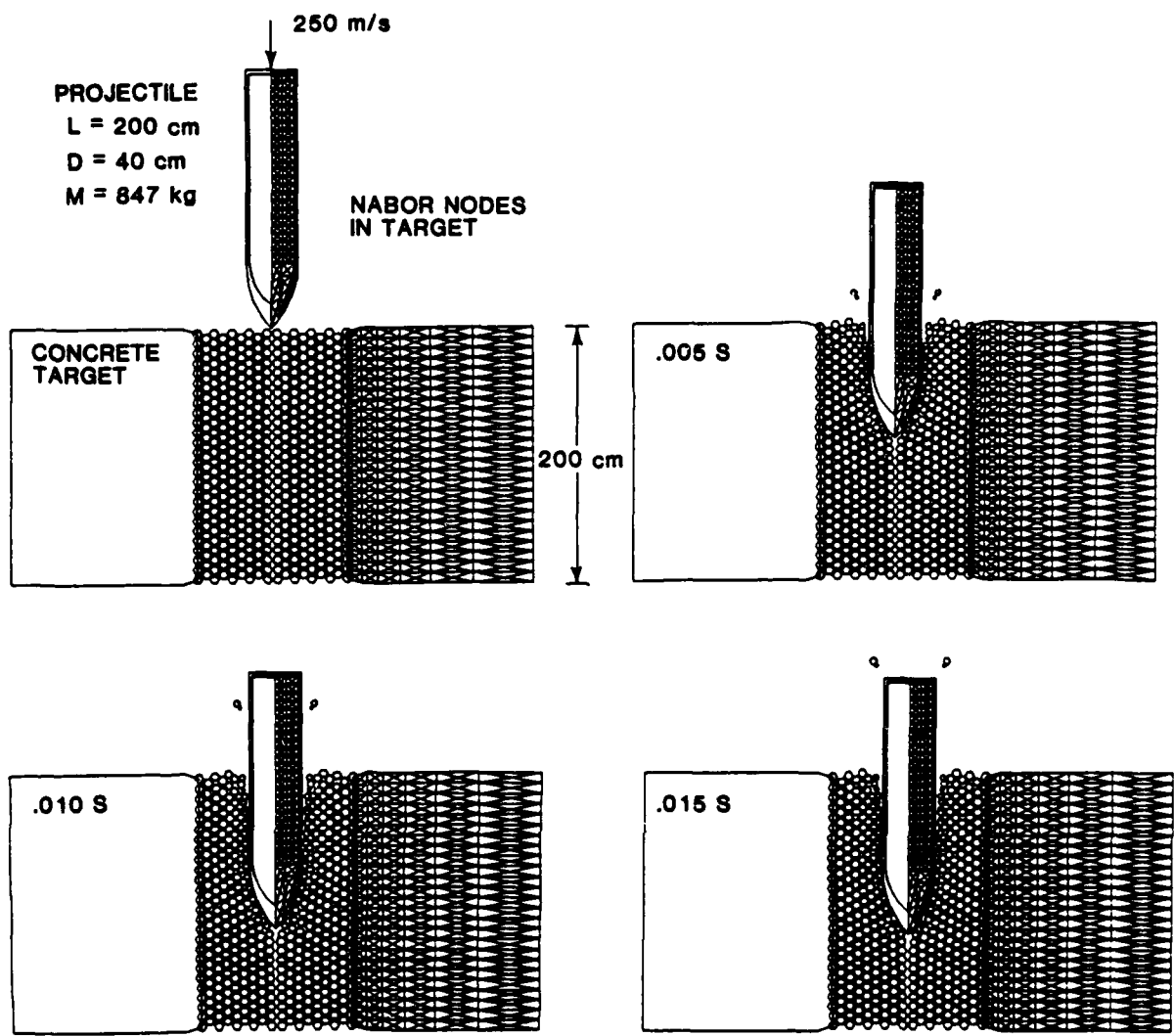


Figure 4. EPIC-2 Computation with NABOR Nodes in Target

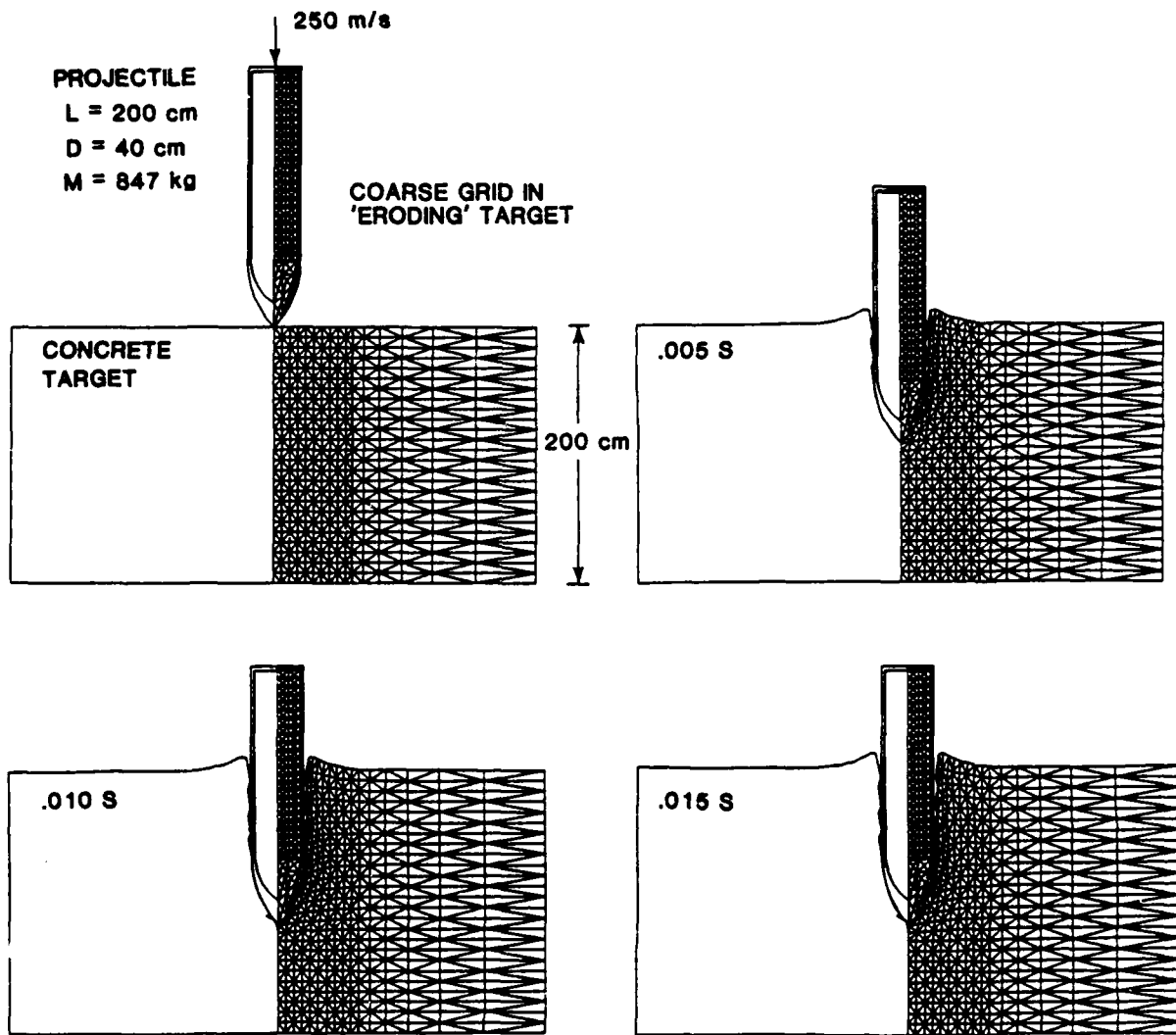


Figure 5. EPIC-2 Computation with Coarse Grid and Erosion in Target

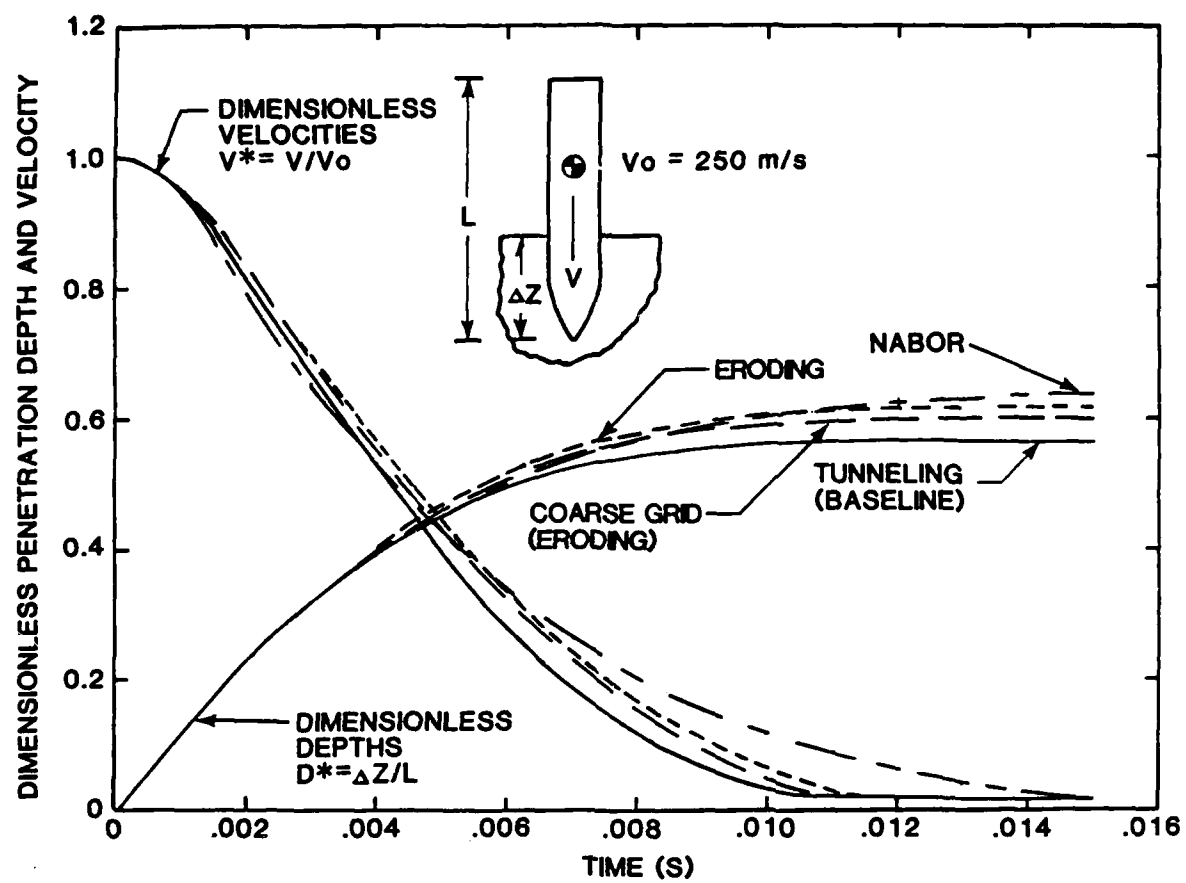


Figure 6. Time Histories of Projectile Penetration Depth and Velocity for the EPIC-2 Computations

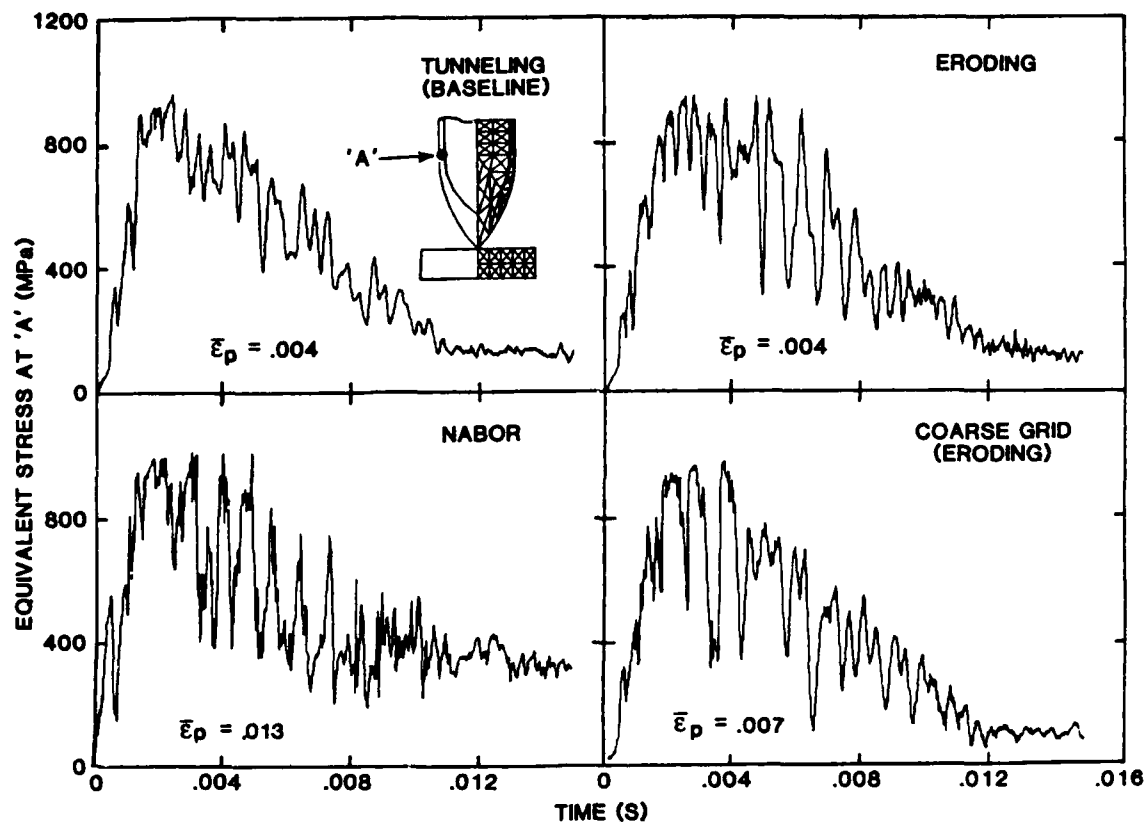


Figure 7. Time Histories of Equivalent Stress in the Projectile Case for the EPIC-2 Computations

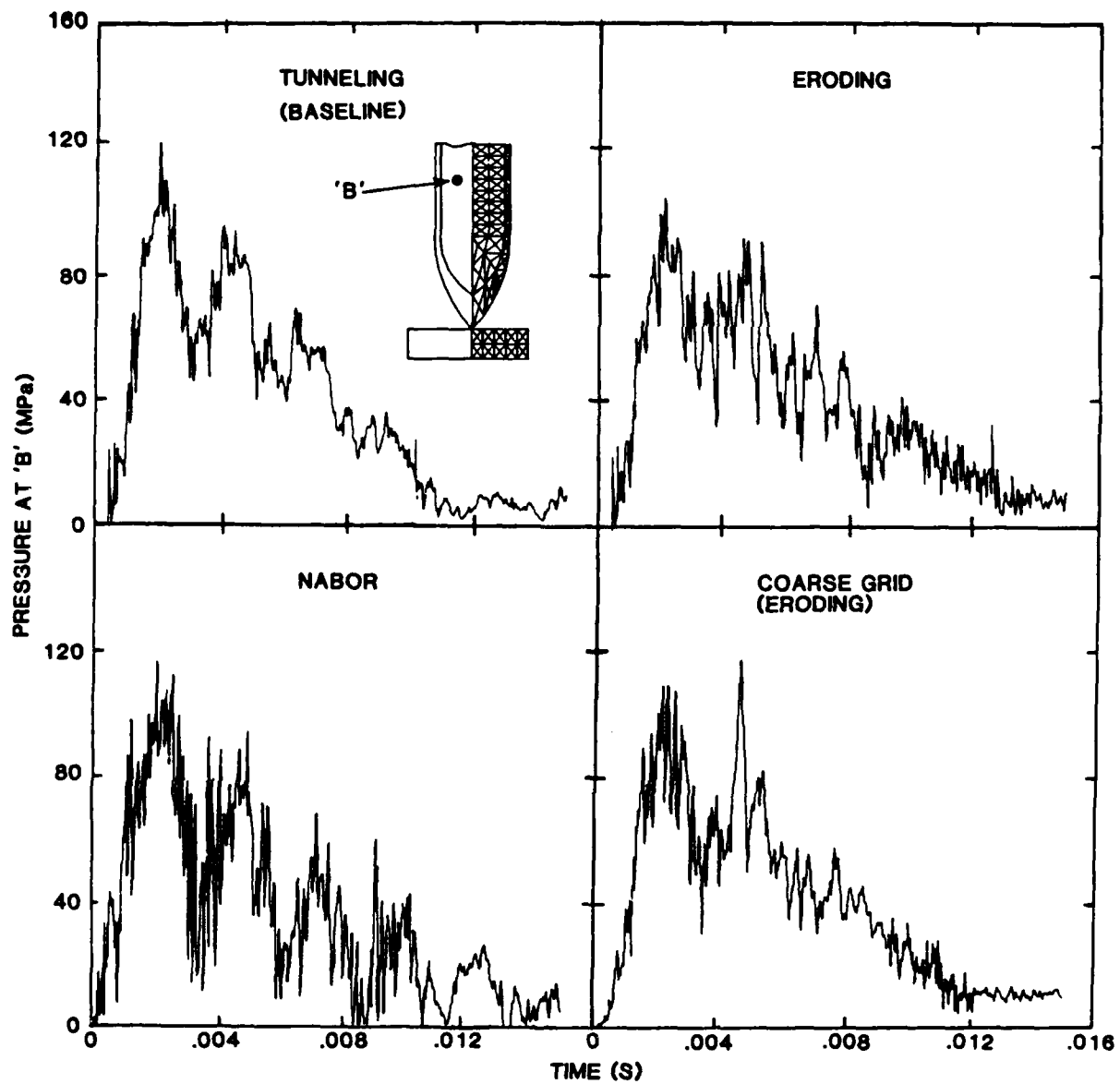


Figure 8. Time Histories of Pressure in the Projectile Explosive for the EPIC-2 Computations

others give similar results. The NABOR computation provides the most deceleration during the initial 0.003 second, but it then decelerates more slowly than the others, and eventually experiences the greatest depth of penetration.

Another comparison is provided in Figure 7, where the equivalent stress at a selected element in the steel case is shown as a function of time. Generally, the responses are very similar and all four cases show a small amount of equivalent plastic strain. The two eroding computations show more oscillation than the tunneling computation, and this is probably due to the instantaneous changes in the resistance of the elements that erode. The NABOR results show a higher stress at later times, and this occurs because the projectile is still decelerating as indicated in Figure 6.

A similar comparison is shown in Figure 8 where the pressure in the inert explosive is shown as a function of time. Again, the general responses are very similar, with the tunneling (baseline) computation having less oscillation than the other responses.

The final comparison is shown in Figure 9, where the acceleration at the top of the projectile case is shown as a function of time. Due to the high frequency responses, it is difficult to make meaningful comparisons. The maximum rigid body deceleration is only 3000-4000 Gs. For the tunneling and the two eroding computations, there appears to be a lower frequency in the range of 0.005 to 0.010 second. During this intermediate time range, the inert explosive is compressed and loses contact with the top of the case. This allows the top of the case to vibrate as a plate, and this probably leads to the lower frequency response. The subsequent higher frequency response is probably due to the inert explosive rebounding back against the end plate of the case.

The NABOR computation provides a noisier signal for all of the time history responses in Figures 7 through 9. The reason for this trend is not obvious.

2. THREE-DIMENSIONAL COMPUTATIONS

Although the two-dimensional axisymmetric computations provide for meaningful comparisons between various computational approaches, the three-dimensional, oblique, and yawed impact problems are of the most interest. The three-dimensional model for the projectile is shown in Figure 1 and the complete model for the erosion computations is shown in Figure 10. The three-dimensional model for a target with NABOR nodes is similar, with the exception that it is rectangular in shape.

Figure 11 shows a three-dimensional computation of the normal impact problem that was previously analyzed in axisymmetric geometry. All of the nodes in the center portion of the target are designated as slave nodes, and the target elements are allowed to erode at an equivalent plastic strain of 1.5. There is no predetermination of penetration path or sliding interfaces.

As shown in the figure, the projectile does not travel in a straight line, as expected, but instead rotates 6 degrees. The initial off-axis perturbation is due to the sliding interface algorithm. If a slave node in the target is exactly positioned on a line connecting two triangular master surfaces, the equations of motion are adjusted in a direction normal to only one of the master surfaces. In the initial geometry, there are numerous occurrences

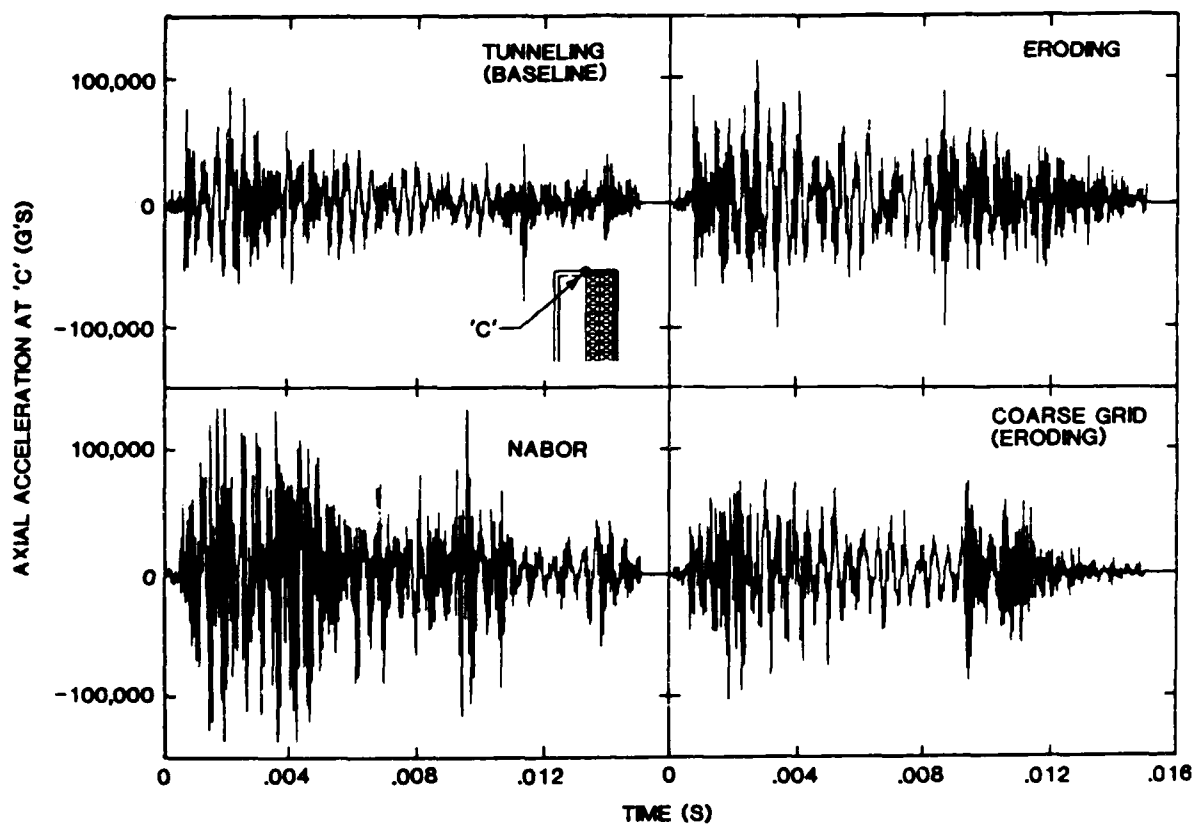


Figure 9. Time Histories of Axial Acceleration at the Aft End of the Projectile for the EPIC-2 Computations

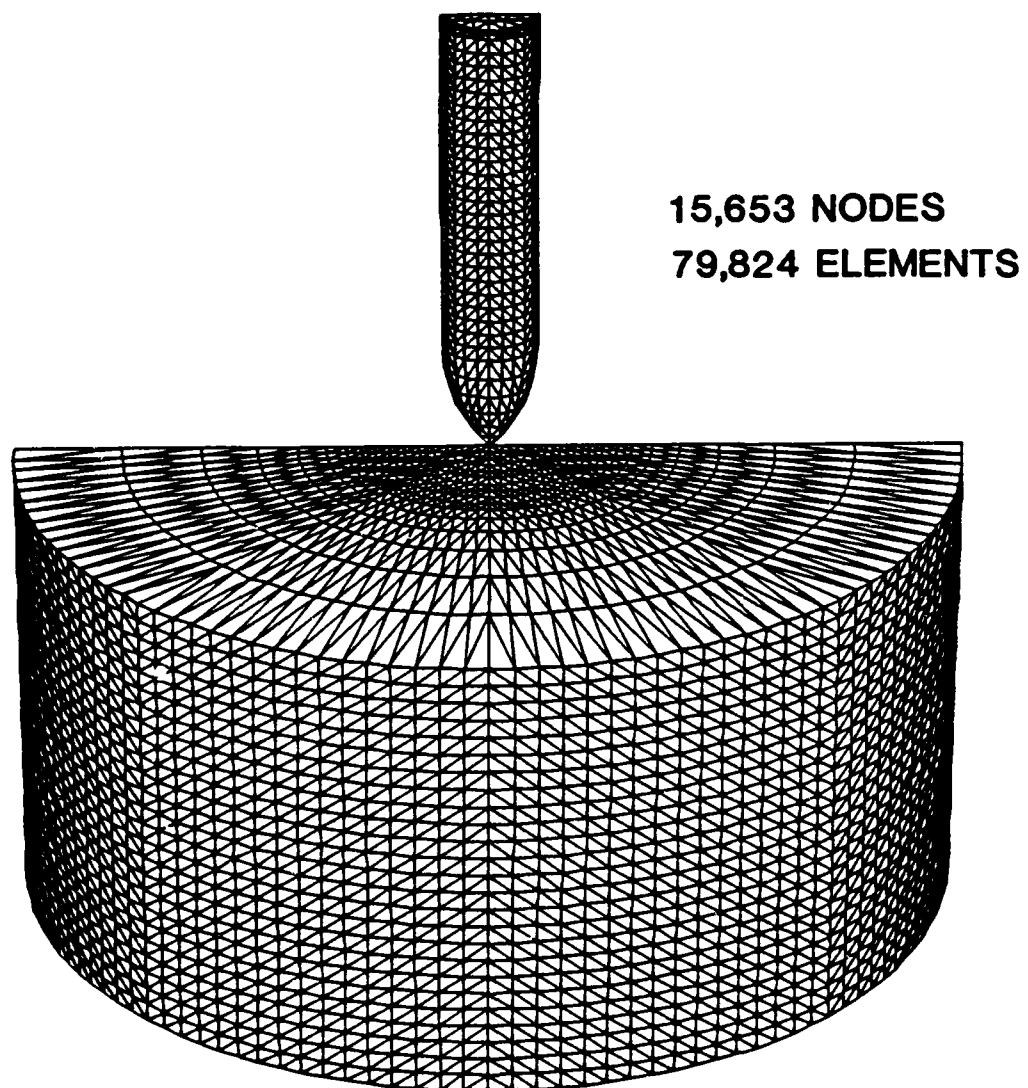


Figure 10. View of the Three-Dimensional, EPIC-3 Grid

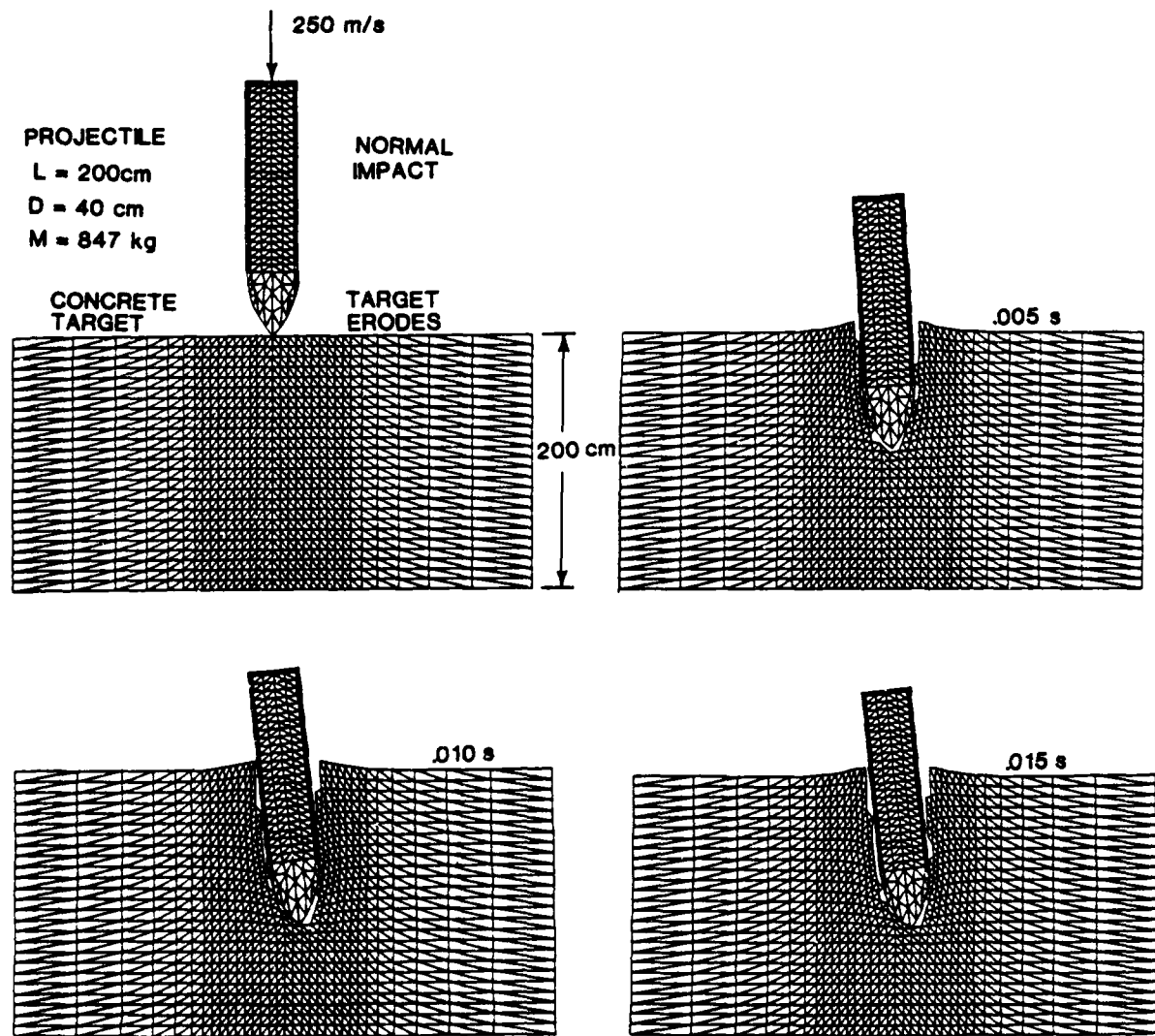


Figure 11. EPIC-3 Computation for Normal Impact, with Erosion in Target

of this match up between slave nodes and master surface interfaces. Although the initial disturbance can be explained, the magnitude of the eventual rotation is surprising.

The maximum penetration depth result is in excellent agreement with the two-dimensional, axisymmetric results. It is only 9 percent greater than the tunneling (baseline) depth of Figure 2, and it falls between the two depths obtained with the eroding target computations of Figures 3 and 5.

Figure 12 shows a three-dimensional NABOR computation of the same normal impact problem. Here, there is a small projectile rotation of 3 degrees, but this rotation is much less than that experienced in the erosion computation of Figure 11. The penetration depth is similar to that of the other computations, being only 1 percent less than the tunneling (baseline) depth of Figure 2.

Penetration depths and velocities for the three-dimensional computations of Figures 11 and 12 are shown in Figure 13. As was the case for the two-dimensional NABOR computations, the three-dimensional NABOR computations also decelerate the projectile at a slightly higher rate than do the other computations. Generally, the three-dimensional computations (eroding, NABOR) show good agreement with the two-dimensional tunneling (baseline) computation.

Figure 14 shows equivalent stresses in selected elements as a function of time. These elements correspond to the element monitored in the two-dimensional computations, as shown in Figure 7. The responses at points A and D should be identical if the responses are truly symmetrical. For the eroding computation, there is a noticeable difference between the responses at the two locations, and this is consistent with the overall projectile rotation as shown in Figure 11. There appears to be more consistency between the two locations for the NABOR computation, and it is probably because the projectile does not experience as much rotation as it does in the eroding computation.

Also, a small amount of plastic strain is experienced at all locations and it is slightly higher for the NABOR computations. This is most likely caused by the higher deceleration as shown in Figure 13.

Although there are some definite differences between the two-dimensional results of Figure 7 and the three-dimensional results of Figure 14, the equivalent stress responses are generally very comparable.

Figure 15 shows pressure as a function of time for the same location monitored in the two-dimensional computations. Here, the responses are very similar at points B and E, and they do not appear to be noticeably affected by the rotation of the projectile. The pressures for the three-dimensional NABOR computation are slightly higher than for the corresponding eroding computation, and this is probably due to the higher deceleration. Again, however, the two-dimensional results of Figure 8 and the three-dimensional results of Figure 15 are generally comparable.

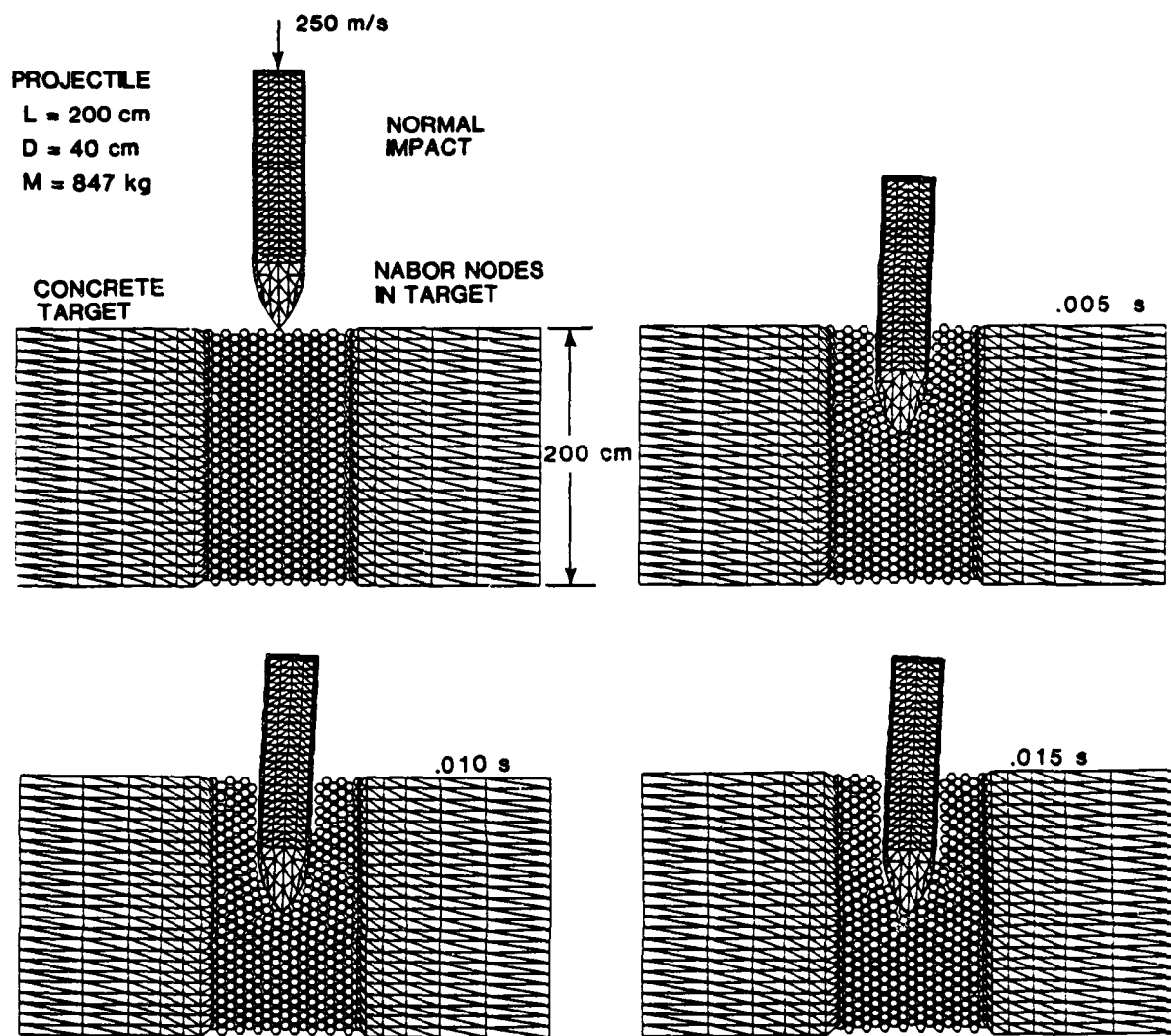


Figure 12. EPIC-3 Computation for Normal Impact, with NABOR Nodes in Target

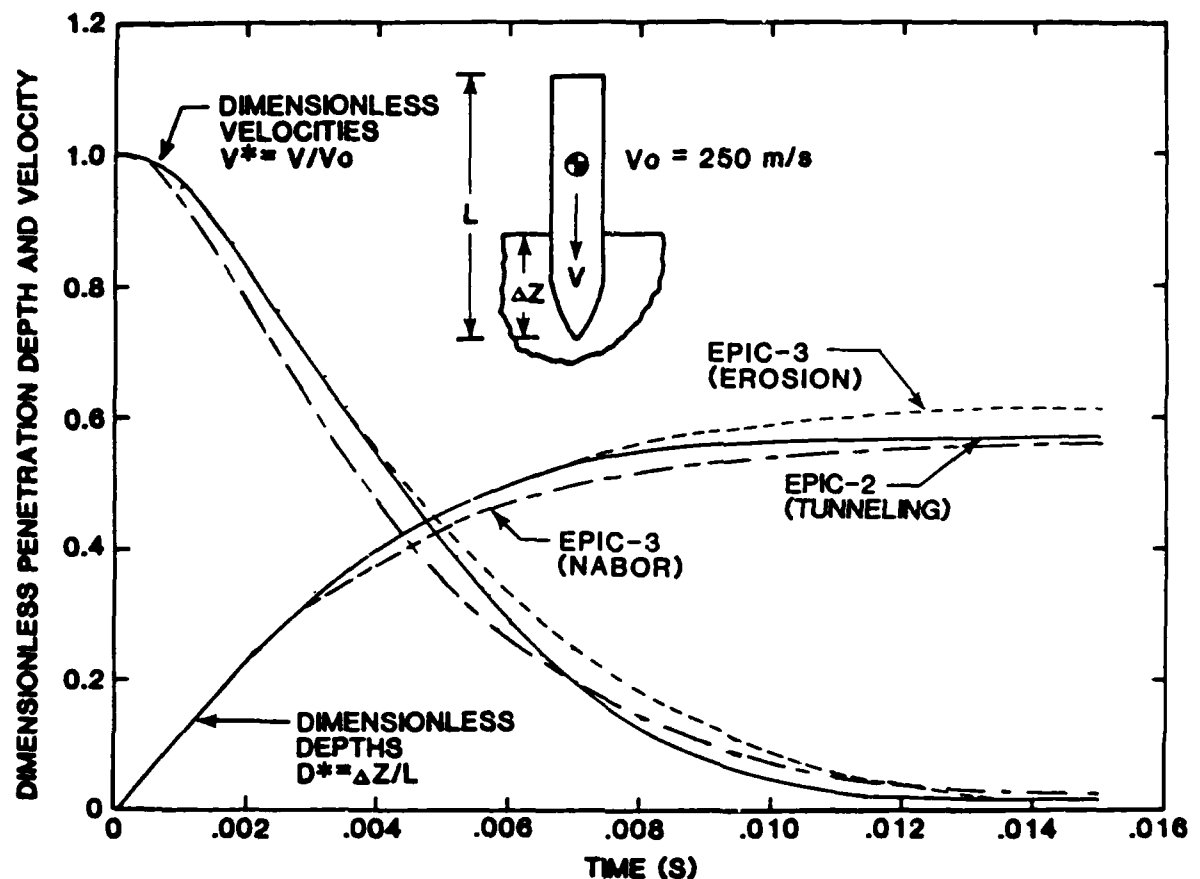


Figure 13. Time Histories of Projectile Penetration Depth and Velocity for EPIC-2 and EPIC-3 Computations

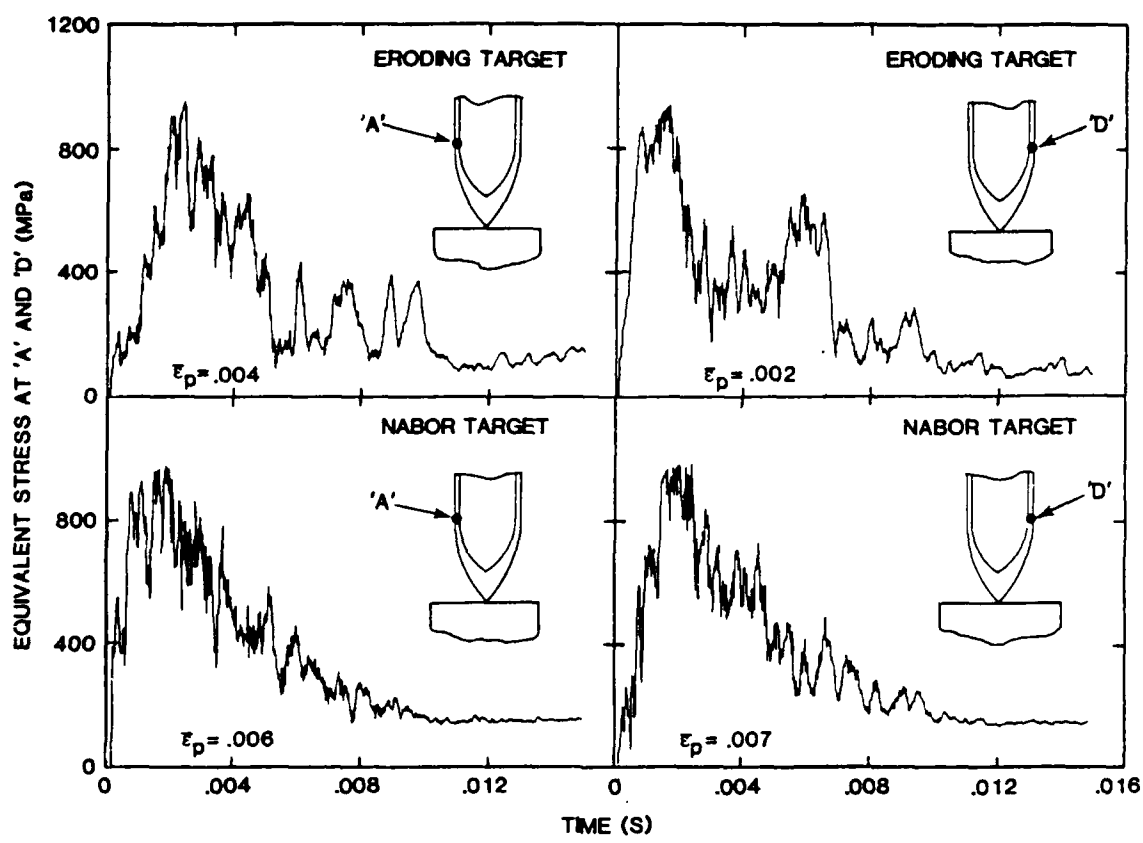


Figure 14. Time Histories of Equivalent Stress in the Projectile Case for the EPIC-3, Normal Impact Computations

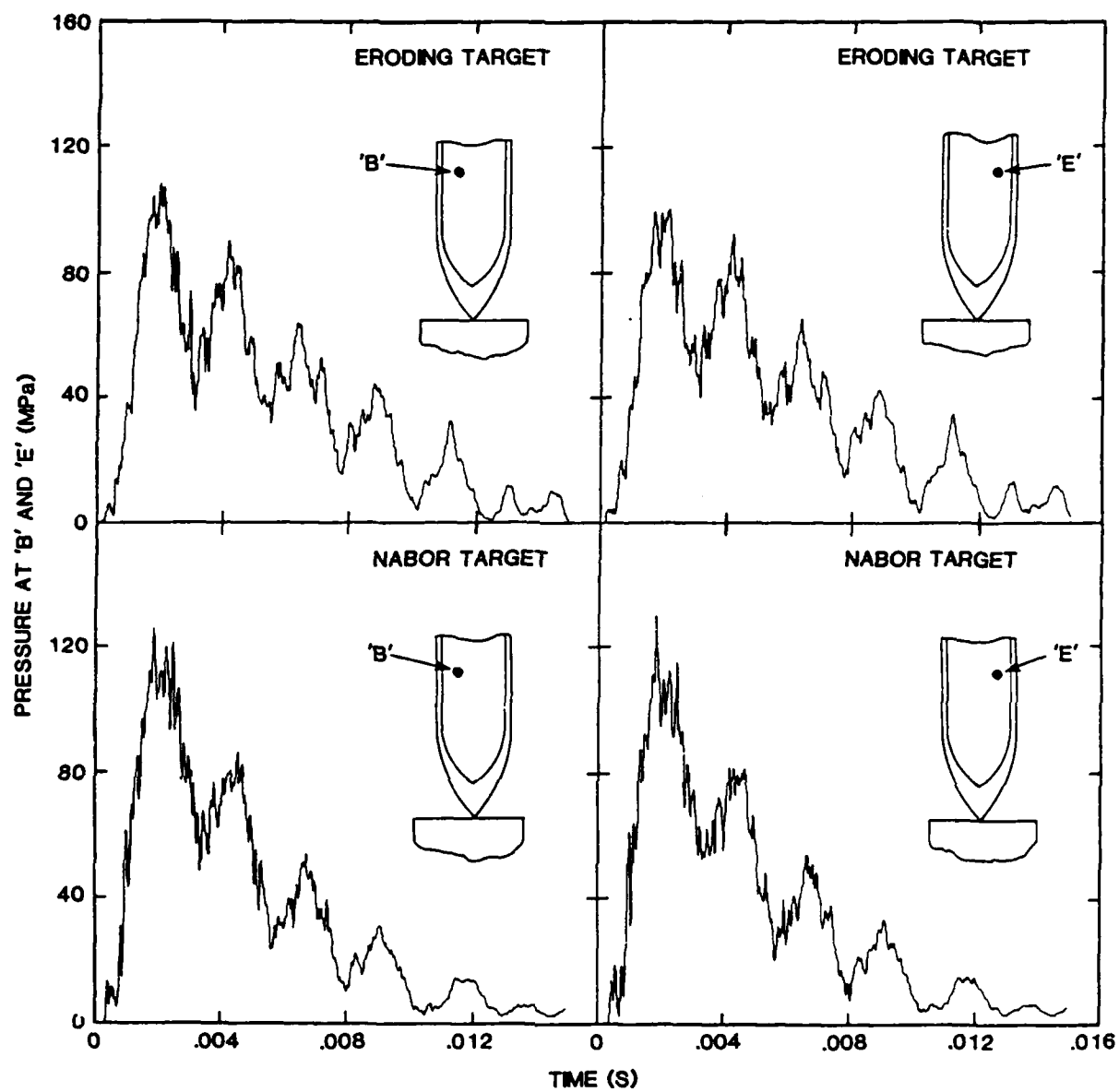


Figure 15. Time Histories of Pressure in the Projectile Explosive for the EPIC-3, Normal Impact Computations

Figure 16 shows acceleration as a function of time at the aft end of the projectile. When the three-dimensional results of Figure 16 are compared to the two-dimensional results of Figure 9, there appears to be a distinct difference. The magnitude of the three-dimensional accelerations is much lower than that experienced in the two-dimensional computations. A possible explanation is that the three-dimensional grid is coarser (it has no center nodes as does the two-dimensional crossed triangles) and cannot develop as high a frequency response as can the two-dimensional grid. Also, a transverse acceleration is developed from the asymmetric response of the projectile.

The three-dimensional, normal impact computations of Figures 11 and 12 have been performed to evaluate the adequacy of the three-dimensional computing techniques. The primary problems of interest involve oblique and/or yawed impact, such as shown in Figures 17 and 18. Both of these computations use the eroding target approach, but it would be expected that the NABOR approach would give similar results.

The oblique impact computation shows the projectile experiencing a significant rotation of 19 degrees, from an initial orientation of 30 degrees to a final orientation of 49 degrees. Similarly, the yawed impact computation goes from an initial orientation of 5 degrees to a final orientation of 16 degrees, for a total rotation of 11 degrees.

The corresponding equivalent stresses and pressures are shown as a function of time in Figures 19 and 20. The equivalent stress at point D rises faster than at point A. This occurs because the compressive axial stress and the compressive bending stress combine at this point during early time. Although the details of these responses vary from those of normal impacts, in some respects they are very similar. The equivalent plastic strains, for instance, are not significantly different from those experienced during normal impact.

The pressures are very similar to those experienced during normal impact, with the pressures at point B being slightly higher than those at point E.

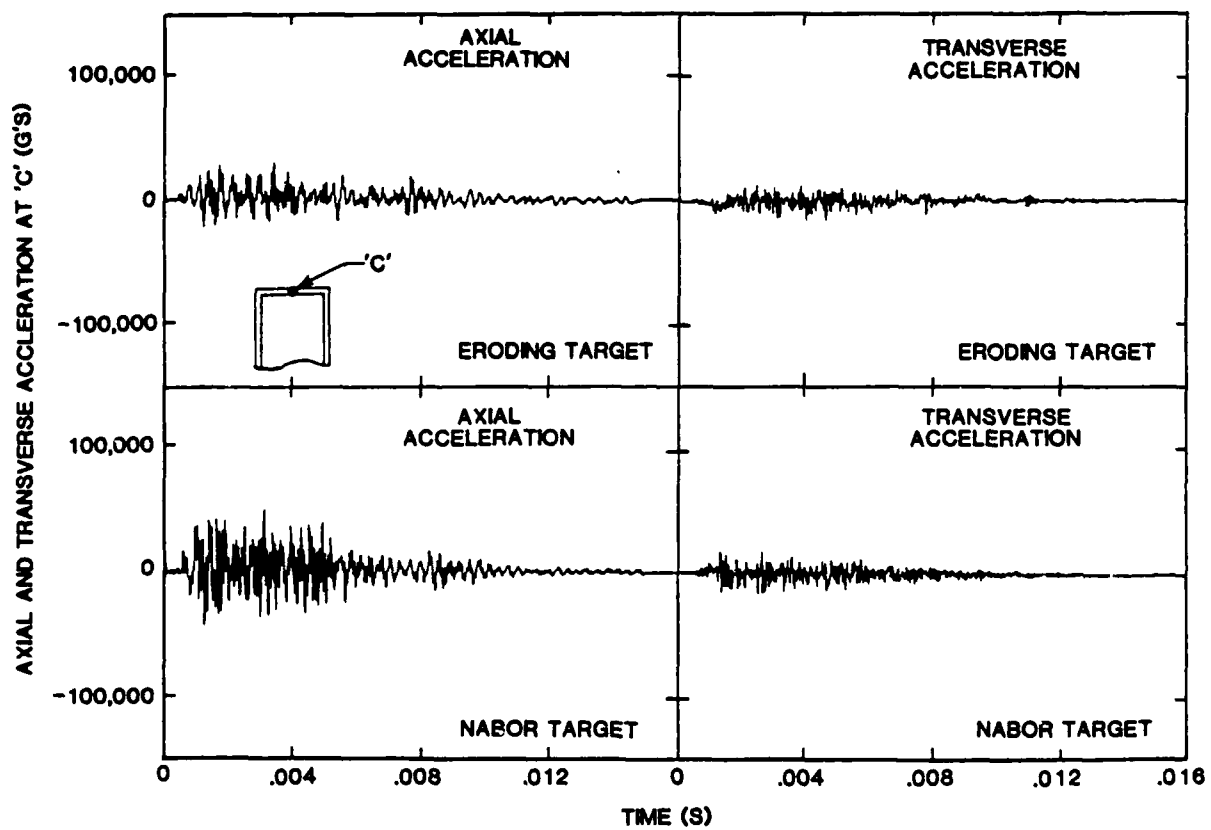


Figure 16. Time Histories of Axial and Transverse Acceleration at the Aft End of the Projectile for the EPIC-3, Normal Impact Computations

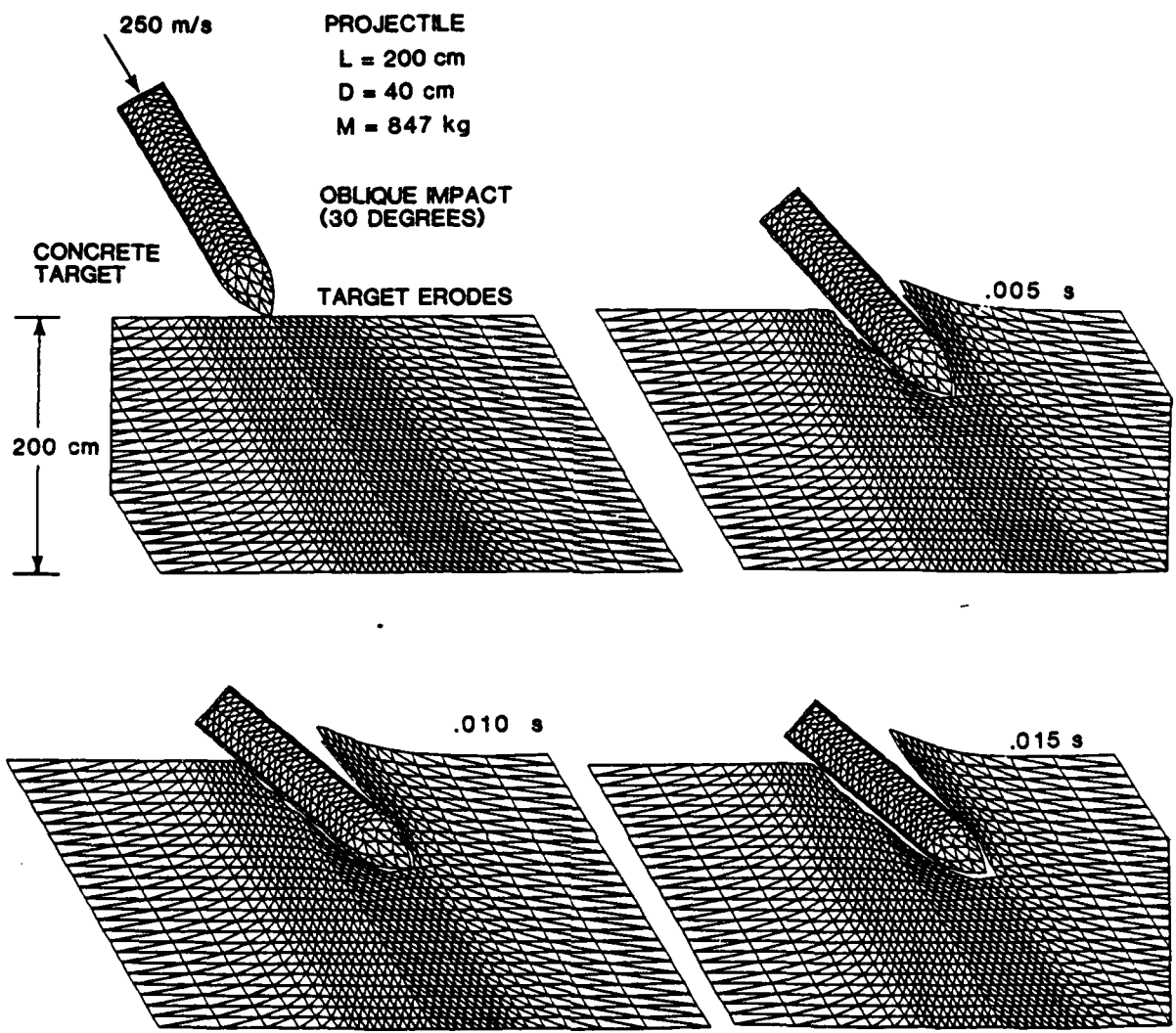


Figure 17. EPIC-3 Computation for Oblique Impact (30 Degrees from Normal) with Erosion in Target

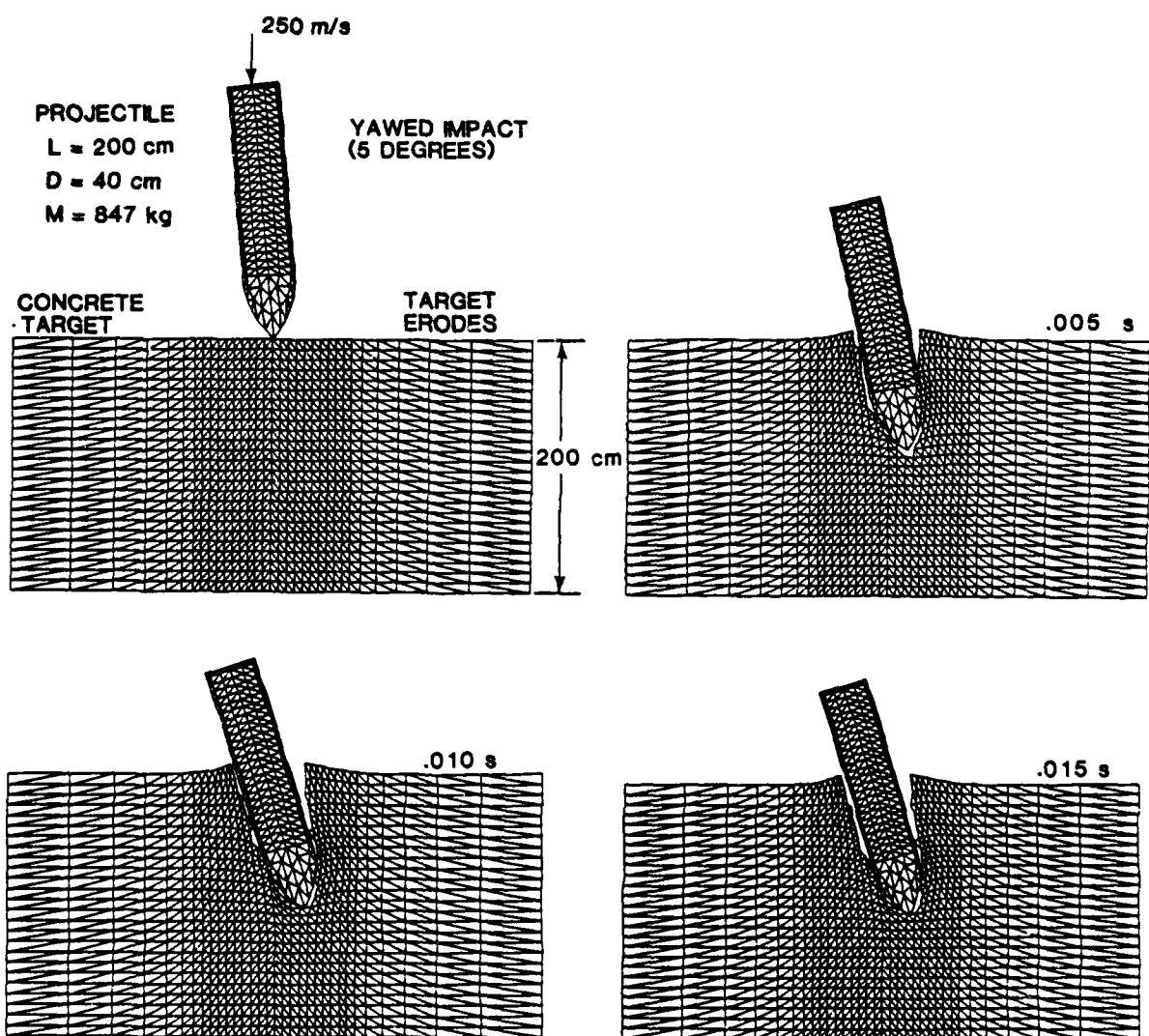


Figure 18. EPIC-3 Computation for Yawed Impact (5 Degrees) with Erosion in Target

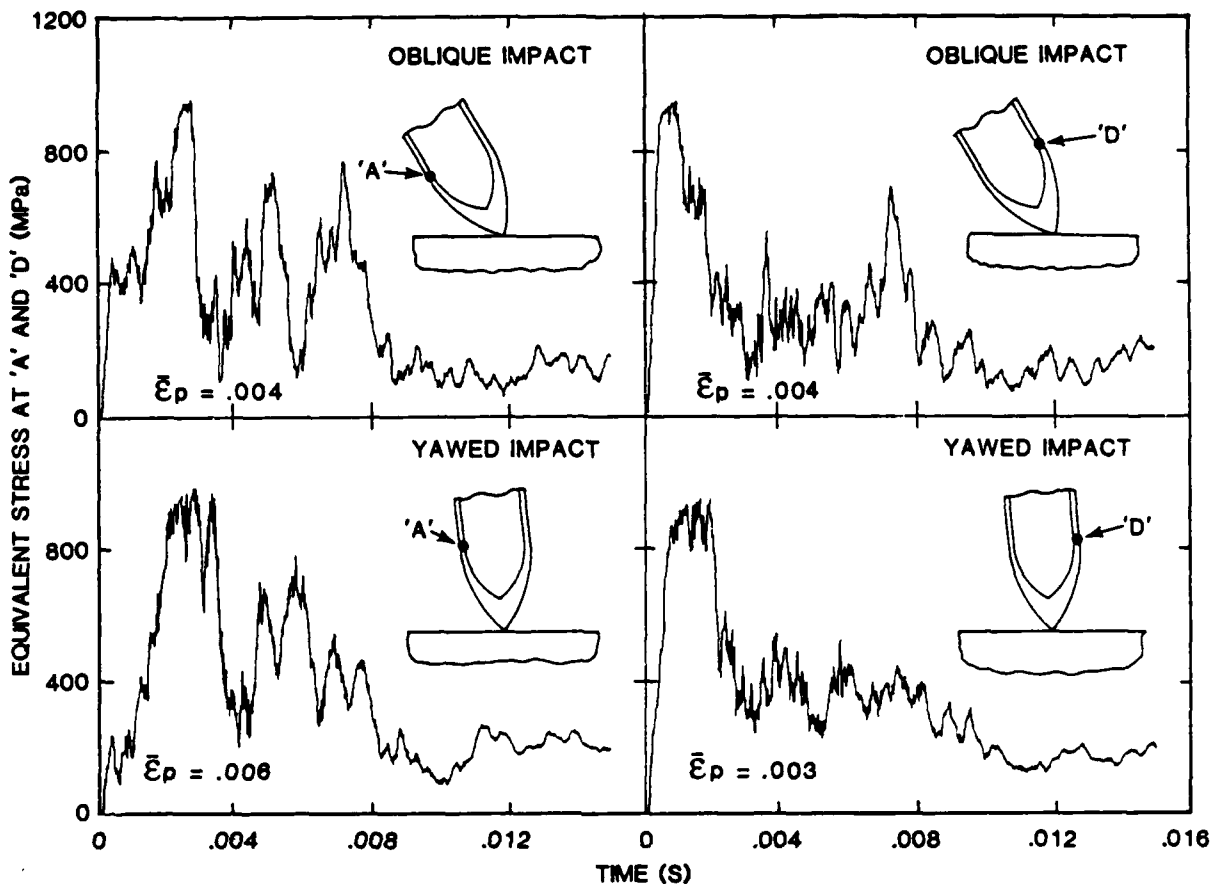


Figure 19. Time Histories of Equivalent Stress in the Projectile Case for the EPIC-3, Oblique and Yawed Impact Computations

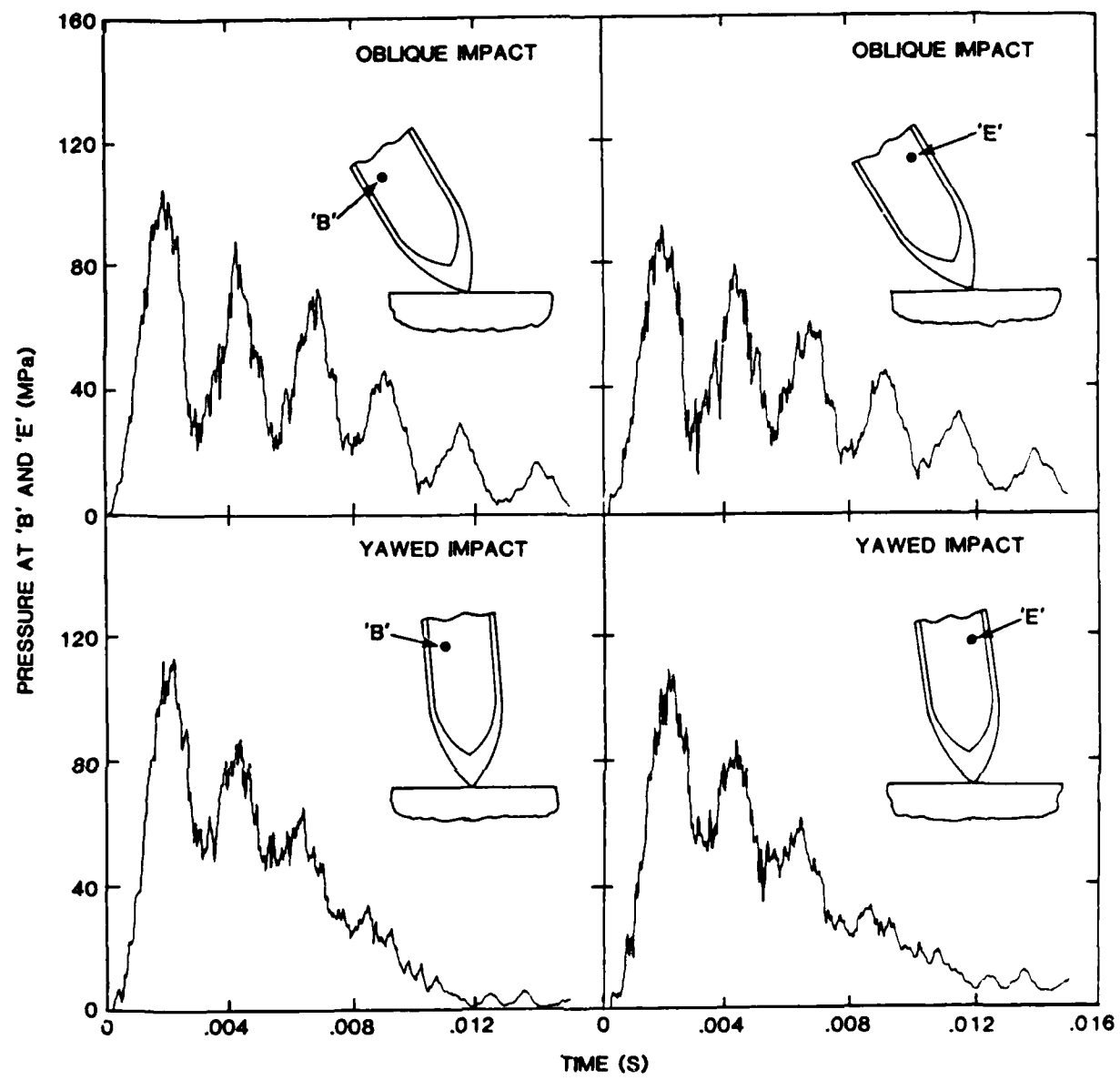


Figure 20. Time Histories of Pressure in the Projectile Explosive for the EPIC-3, Oblique and Yawed Impact Computations

SECTION III NABOR ALGORITHMS

This section presents the specific algorithms for both the axisymmetric and the three-dimensional NABOR techniques. These are the algorithms used for the computations in Figures 4 and 12 in the preceding section. These are Lagrangian algorithms because the material moves with the grid. The distinguishing feature of these approaches is that they allow for variable nodal connectivity.

The NABOR technique was first demonstrated in plane strain geometry during the early phases of this contract (Reference 9). Based on those results, it was then extended to axisymmetric and three-dimensional geometry. It should be noted that the idea of variable nodal connectivity is not new. A Particle-and-Force (PAF) method was developed for fluids in the early 1960's by Daly, Harlow and Welch (Reference 10). Although there are some similarities in the general approaches of the PAF and NABOR algorithms, they are quite different.

A schematic representation of a plane strain NABOR grid for an impact problem is shown in Figure 21. The NABOR nodes are somewhat analogous to circular flexible disks. The equilibrium position is a hexagonal close-pack, where each internal node has six neighbors. As node j moves closer to node i , a compressive, repulsive force is exerted on node i , as shown in the lower portion of Figure 21. (This force also acts on node j .) Node k is moving away from node i and, therefore, exerts a tensile, attractive force on node i . Variable connectivity is also demonstrated in Figure 21, where node m is moving inward to become a neighbor of node i , and node j is moving outward to eventually have no effect on node i .

1. AXISYMMETRIC GEOMETRY

The axisymmetric geometry is similar to the plane stress geometry, with the complicating exceptions that the hoop strains, strain rates, and stresses must all be considered. The mass of a NABOR node for axisymmetric geometry is

$$M = \pi \sqrt{3} r_o \rho_o D_o^2 \quad (1)$$

where r_o is the initial radial coordinate at the center of the node, ρ_o is the density of the material, and D_o is the initial diameter of all NABOR nodes contained in the specific problem.

a. Strains and Strain Rates

Figure 22 shows a bond between NABOR nodes i and j . D is the current distance between nodes, and \dot{u}_i and \dot{v}_i are the r and z velocities of node i . V_i^N is the normal velocity vector along the bond at node i , and V_i^P is the velocity vector perpendicular to the bond. The following equations represent various strains and strain rates.

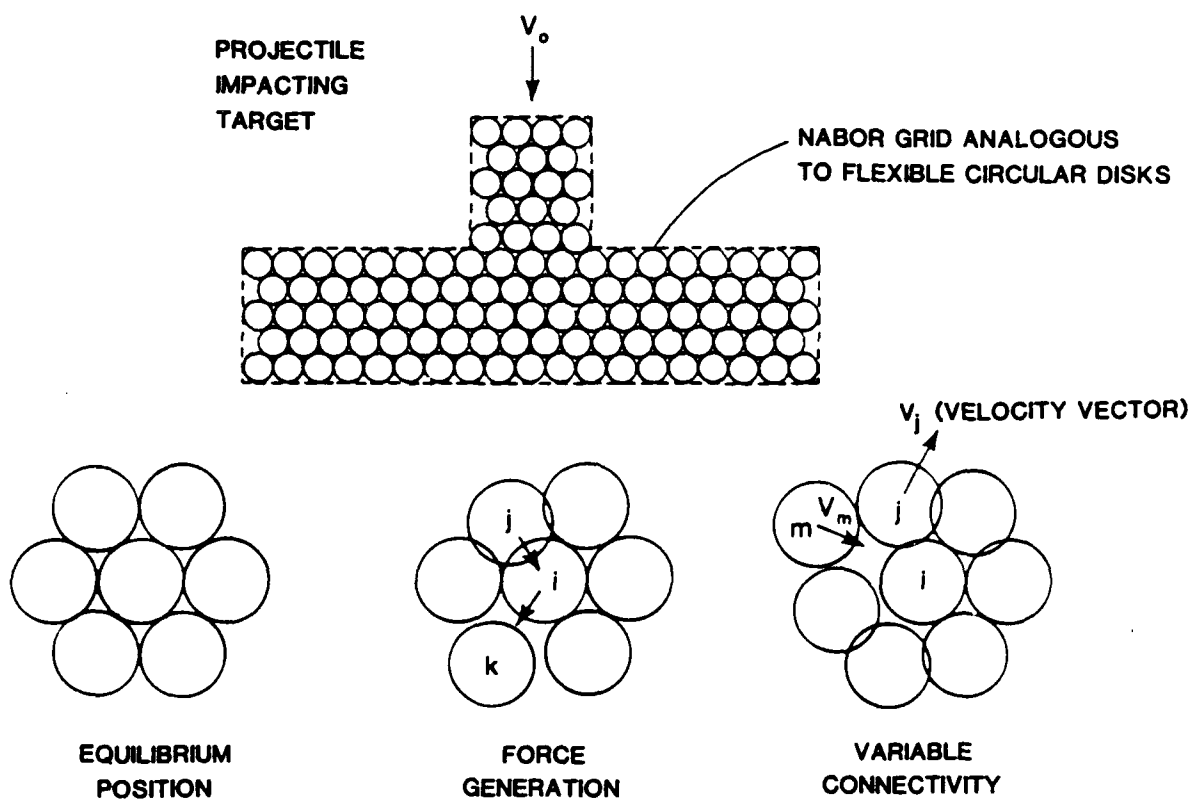
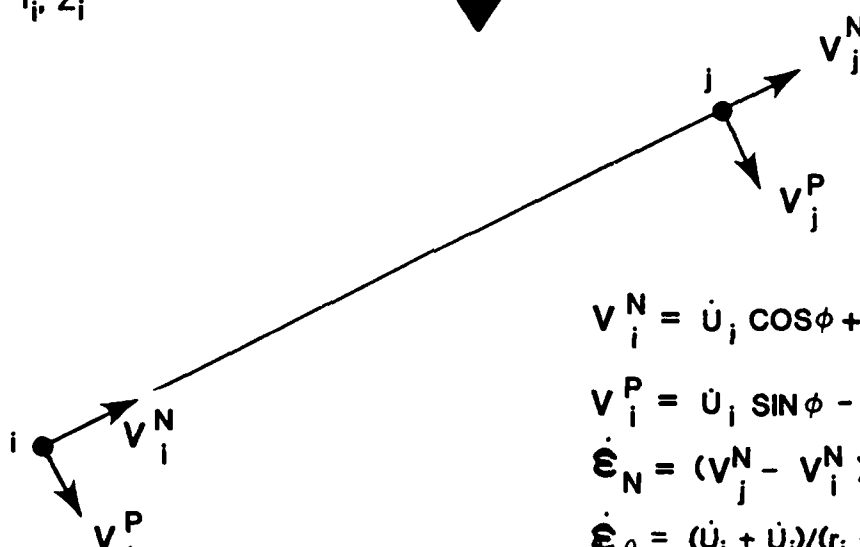
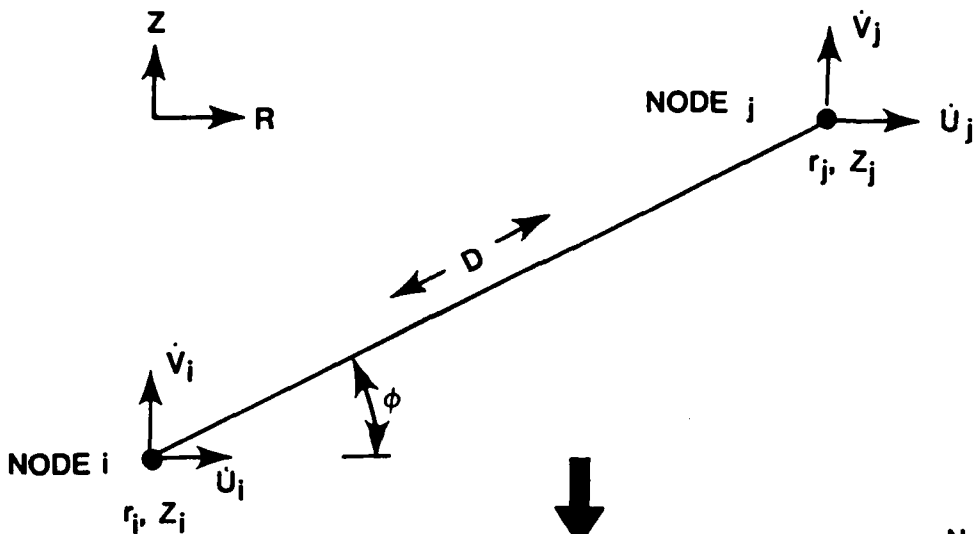


Figure 21. Schematic Representation of the NABOR Computational Technique in Plane Strain Geometry



$$v_i^N = \dot{U}_i \cos\phi + \dot{V}_i \sin\phi$$

$$v_i^P = \dot{U}_i \sin\phi - \dot{V}_i \cos\phi$$

$$\dot{\epsilon}_N = (v_j^N - v_i^N)/D$$

$$\dot{\epsilon}_\theta = (\dot{U}_i + \dot{U}_j)/(r_i + r_j)$$

$$\dot{\gamma} = (v_j^P - v_i^P)/D$$

Figure 22. Definition of Velocities and Strain Rates for Axisymmetric Geometry

$$\dot{\varepsilon}_N = (V_j^N - V_i^N)/D \quad (2)$$

$$\dot{\varepsilon}_\theta = (\dot{u}_i + \dot{u}_j)/(r_i + r_j) \quad (3)$$

$$\dot{\varepsilon}_p = \beta(\dot{\varepsilon}_N + \dot{\varepsilon}_\theta) \quad (4)$$

$$\dot{\gamma} = (V_j^P - V_i^P)/D \quad (5)$$

$$\bar{\dot{\varepsilon}} = \sqrt{\frac{2}{9} \left[(\dot{\varepsilon}_N - \dot{\varepsilon}_p)^2 + (\dot{\varepsilon}_N - \dot{\varepsilon}_\theta)^2 + (\dot{\varepsilon}_p - \dot{\varepsilon}_\theta)^2 + \frac{3}{2} \dot{\gamma}^2 \right]} \quad (6)$$

$$\bar{\varepsilon} = \sum \alpha \bar{\dot{\varepsilon}} \Delta t / N \quad (7)$$

The strain rates along the bond, perpendicular to the bond, and in the hoop direction are given by $\dot{\varepsilon}_N$ and $\dot{\varepsilon}_p$, and $\dot{\varepsilon}_\theta$, respectively. While $\dot{\varepsilon}_N$ and $\dot{\varepsilon}_\theta$ can be exactly defined, $\dot{\varepsilon}_p$ must be approximated.

It will later be shown that β is often within the range, $-1 < \beta < 0$, and it is therefore assumed that $\beta = -0.5$. The shear strain rate, $\dot{\gamma}$, is also an approximation inasmuch as three nodes (rather than two) are required to give an exact description.

The equivalent strain rate, $\bar{\dot{\varepsilon}}$, can be integrated to give an approximate equivalent strain, $\bar{\varepsilon}$. In Equation 7, Δt is the integration time increment, and α is a factor that varies linearly from 0 at $D = 1.3D'_o$ to 1.0 for $D \leq 1.15D'_o$. This α factor is also applied to stresses and pressures; it provides for a smooth transition at $D = 1.3D'_o$ and lessens the influence of nodes at extended bond distances.

N is the number of bonds (neighbor nodes) at the NABOR node, where a bond is defined as two nodes with a distance between them of $D \leq 1.3D'_o$. The other term is $D'_o = D_o \sqrt{r_o/r}$. It is the effective, unstrained nodal diameter in the r - z plane, caused by the current radial coordinate, r , being different from the initial radial coordinate, r_o .

Although $\bar{\varepsilon}$ is updated from a bond strain rate, $\bar{\dot{\varepsilon}}$, it must be carried from cycle to cycle as a nodal quantity. The increment of nodal strain is, therefore, the average of all the incremental bond strains associated with that node. Because the nodal connectivity can vary from cycle to cycle, there can be no retention of bond variables; only the nodes can retain variables from cycle to cycle.

The volumetric strain for pressure computations is $\mu = \rho/\rho_o - 1 = V_o/V - 1$, where ρ_o and ρ are the initial and current densities of a specified element of material, and V_o and V are the corresponding volumes. Because a two-dimensional volume cannot be determined from the distance between two nodes, μ is determined from:

$$\mu_1 = \bar{D}'_o/D - 1.1547 \quad (8a)$$

$$\mu_2 = (D_o/\bar{D})^2 - 1 \quad (8b)$$

$$\mu = \max(\mu_1, \mu_2) \quad (8c)$$

Equation 8a insures that two nodes cannot get too close together. The constant in this equation (1.1547) allows pure shear to occur without introducing a significant volumetric strain. This also reduces the locking and cracking problems associated with the initial plain strain NABOR algorithm (Reference 9). In equation 8b, $\bar{D} = \Sigma D (D_o/D'_o)/N$ is the average factored distance to all of the neighbor nodes with $D \leq 1.3D'_o$. Similarly, D'_o is the average of D'_o for the two nodes forming the bond.

Figure 23 shows the necessity for μ_2 . The initial hexagonal geometry is uniformly strained in the vertical direction only. Furthermore, it is assumed that $D'_o = D_o$ for all nodes. Therefore, μ should be identical for all bonds. This is clearly not the case for μ_1 ; the distance between nodes i and j is greater than the distance between nodes i and k. The computed μ , is incorrect for both cases. Fortunately, the nodal quantity, $\mu \approx \sigma/h$, is essentially correct for small volumetric strains. In equation 8c, $\bar{\mu}_2$ is the average of the two nodal volumetric strains.

Another geometric distance that will be used later for the force computations is

$$D_p = (\bar{D}'_o)^2/D (1 + \mu) \quad (9)$$

where D_p is a representative nodal distance in the direction perpendicular to the bond distance, D .

b. Deviator and Shear Stresses

The deviator and shear stresses are dependent on the strains and strain rates in Equations 2-7. Because the strains and strain rates are based on approximations, the deviator and shear stresses are also approximately determined. Only plastic flow is considered and elastic effects are not included. The deviator stresses in the normal (along the bond), and hoop directions, and the shear stress are given by

$$s_N = 2\alpha \bar{\sigma} \dot{e}_N / 3\bar{\epsilon} \quad (10)$$

$$s_\theta = 2\alpha \bar{\sigma} \dot{e}_\theta / 3\bar{\epsilon} \quad (11)$$

$$\tau = \alpha \bar{\sigma} \dot{\gamma} / 3\bar{\epsilon} \quad (12)$$

where $\bar{\sigma}$ is the equivalent tensile flow stress, and \dot{e}_N and \dot{e}_θ are deviator strain rates. The equivalent tensile flow stress in the EPIC codes (References 1 and 2) is expressed as a function of the strain, strain rate, temperature and/or pressure.

The deviator and shear stresses are dependent on strain rates, which have been approximated in some instances. Assuming $\dot{e}_\theta = 0$, the effect of setting $\beta = -0.5$ in Equation 3 is shown in Figure 24. For incompressible plastic flow, $\dot{e}_p = -\dot{e}_N$ so that $\beta = -1.0$. On the other extreme, $\beta = 0$ for one-dimensional wave propagation along \dot{e}_N . Fortunately, s_N is not very sensitive to β in this range, and the assumption that $\beta = -0.5$ is acceptable.

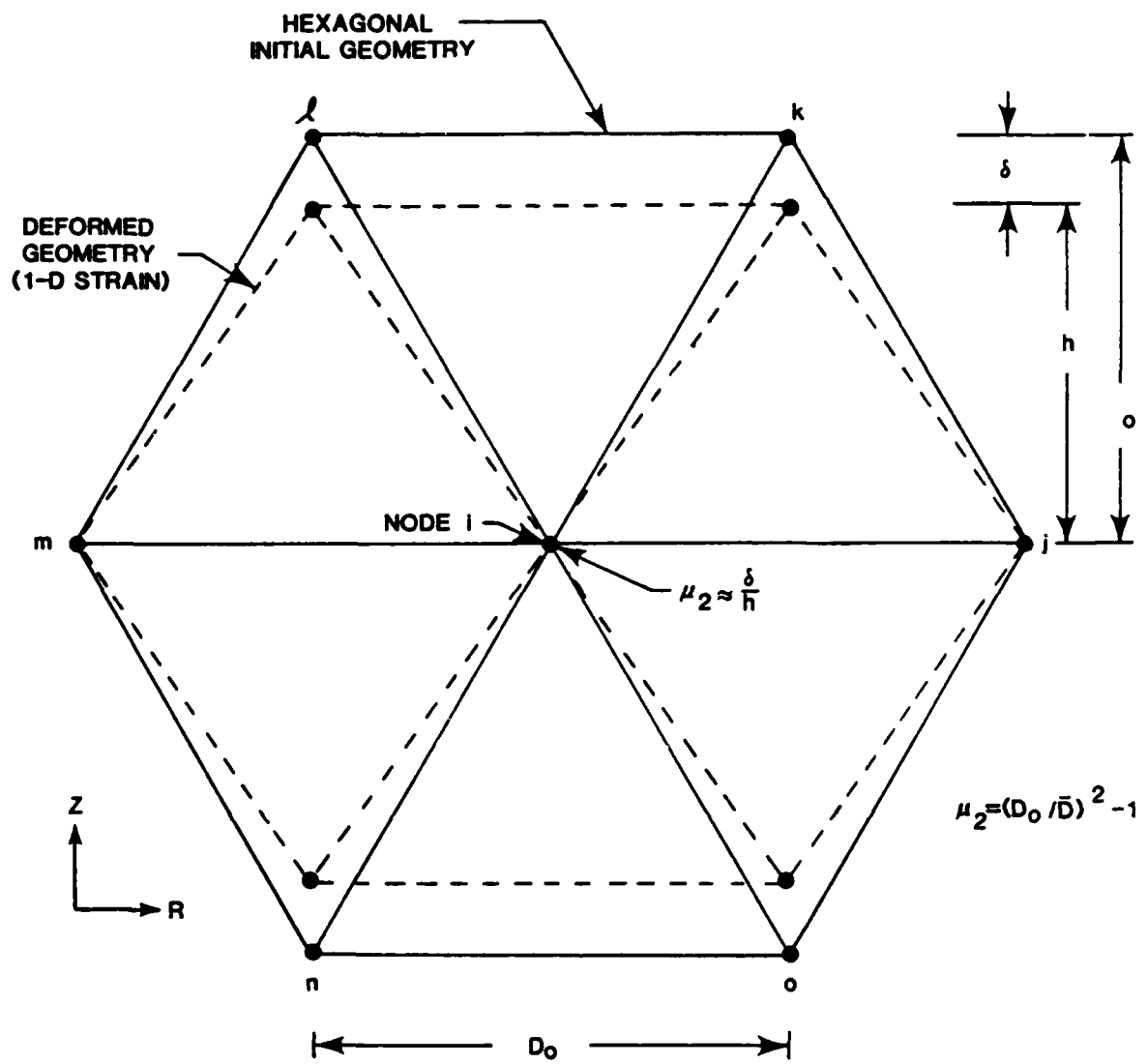


Figure 23. Volumetric Strains for One-Dimensional Compression

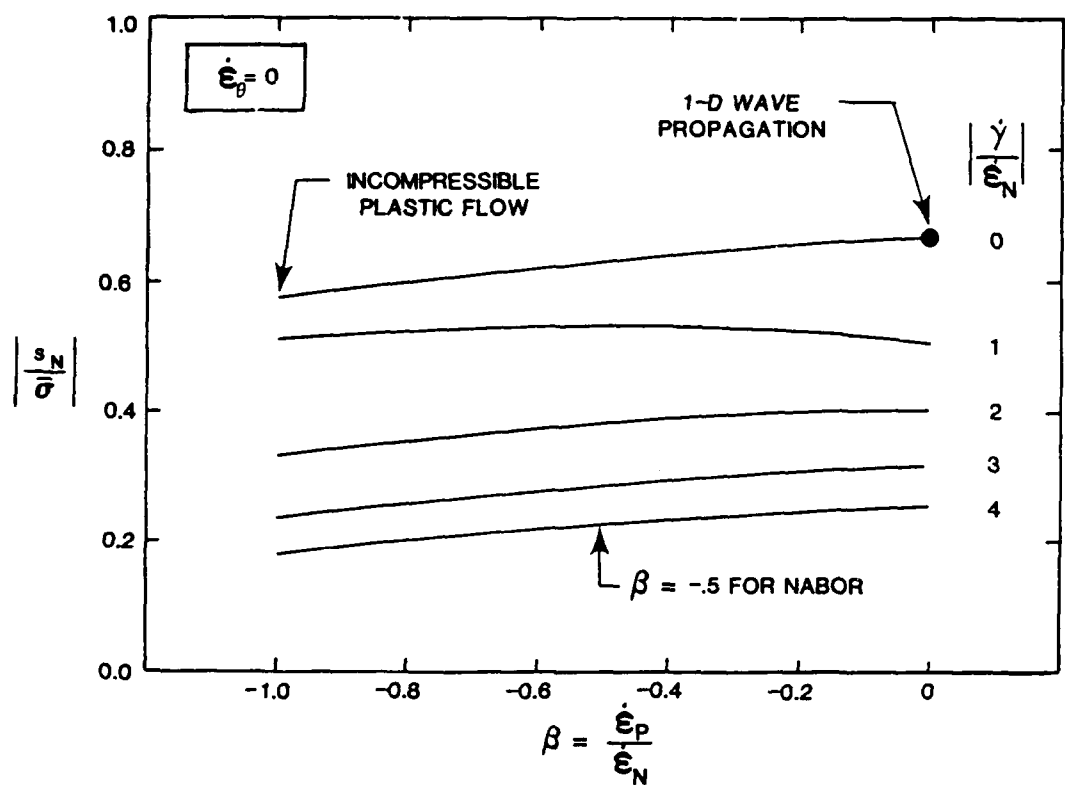


Figure 24. Plastic Flow Relationships for Various Strain Rates

c. Pressure and Artificial Viscosity

The total normal stress along the bond and the hoop stress are

$$\sigma_N = s_N - (P + Q) \quad (13)$$

$$\sigma_\theta = s_\theta - (P + Q) \quad (14)$$

where s_N and s_θ are the previously defined deviator stresses, P is the hydrostatic pressure and Q is the artificial viscosity. Compression is positive for P and Q . The artificial viscosity damps out localized oscillations that would otherwise occur during wave propagation (Reference 11).

$$Q = C_L \rho c_s D |\dot{\varepsilon}_V| + C_Q \rho D^2 \dot{\varepsilon}_V^2 \quad \text{for } \dot{\varepsilon}_V < 0 \quad (15)$$

$$Q = 0 \quad \text{for } \dot{\varepsilon}_V \geq 0$$

where C_L and C_Q are dimensionless coefficients, c_s is the sound velocity, $\dot{\varepsilon}_V$ is the volumetric strain rate and the other terms are as previously defined.

The pressure is determined from the Mie-Gruneisen equation of state (Reference 12). For compressive strains ($\mu > 0$)

$$P = (K_1\mu + K_2\mu^2 + K_3\mu^3)(1 - \Gamma\mu/2) + \Gamma\rho E \quad (16)$$

where K_1 , K_2 , K_3 and Γ are material-dependent constants and E is internal energy per unit mass. At high pressures, the pressure can be significantly affected by the internal energy. Therefore, it is necessary to solve the pressure and energy equations simultaneously. Equation 16 can be rewritten as

$$P^{t+\Delta t} = P_H + \Gamma\rho E^{t+\Delta t} \quad (17)$$

where

$$P_H = (K_1\mu + K_2\mu^2 + K_3\mu^3)(1 - \Gamma\mu/2) \quad (18)$$

$$E^{t+\Delta t} = E^t + \Delta E_s + (\bar{F}\Delta D\bar{N} + \bar{F}_i^R\Delta R_i N_i + \bar{F}_j^R\Delta R_j N_j)/(M_i + M_j) \quad (19)$$

The superscripts t and $t + \Delta t$ represent the times at the beginning and end of an integration cycle. In Equation 19, ΔE_s is the increment of internal energy per unit mass generated by the shear and deviator stresses during the current integration cycle. In the same equation, \bar{N} is the average number of neighbor nodes of the two nodes forming the bond, \bar{F} is the average force (from P and Q only) acting at that bond, and $\Delta D = D\dot{\varepsilon}_N\Delta t$ is the distance through which the force acts. The other forces (\bar{F}_i^R , \bar{F}_j^R), distances (ΔR_i , ΔR_j), and numbers of neighbor nodes (N_i , N_j) are for the hoop components. The masses of the two nodes are M_i and M_j .

The average forces (\bar{F} , \bar{F}_i^R , \bar{F}_j^R) are functions of $(P + Q)^t$ and $(P + Q)^{t + \Delta t}$. The specific force-stress relationships will be presented later. Because $(P + Q)^t$ is known from the previous cycle, and $Q^{t + \Delta t}$ is known from the current cycle, the only unknown on the right side of Equation 19 is $P^{t + \Delta t}$. Substituting Equation 19 into Equation 17 gives an explicit equation for $P^{t + \Delta t}$ that is consistent with $E^{t + \Delta t}$.

There are two significant assumptions associated with \bar{N} and \bar{F} . They are related to the fact that a single node usually has more than one neighbor, and therefore, more than one bond. When this occurs, it is assumed that the other bonds generate the same amount of energy as the specific bond being considered. This assumption is performed by the presence of \bar{N} .

The next assumption concerns \bar{F} . In the force-stress relationships, $(P + Q)^t$ is a nodal quantity, which is the average of $(P + Q)$ for all the individual bonds at time = t . As mentioned previously, it is not possible to carry bond variables from cycle to cycle because the nodal connectivity is not fixed. Therefore, the nodal quantity $(P + Q)^t$ will not be the exact bond quantity at time = t . This approximation tends to reduce $(P + Q)^t$ at the bonds where the pressure is the highest and where the most internal energy is generated. As a result of this reducing assumption, the computed internal energy is sometimes too low, and this leads to a computed energy loss (internal and kinetic) for the entire system.

For expanded states ($\mu < 0$), $K_2 = K_3 = 0$ and the maximum negative pressure is limited to a fraction (about half) of the strength of the material, $\bar{\sigma}$. Furthermore, the tensile pressure $(P + Q)$ is multiplied by α . This gives a smooth transition of $\alpha(P + Q) = 0$ at $D = 1.3D'_o$.

d. Concentrated Forces

The concentrated forces acting on the nodes are statically equivalent to the normal, hoop, and shear stresses (σ_N , σ_θ , τ). The comparable normal, hoop, and shear forces (F_N , F_θ , F_p) are shown in Figure 25 and are expressed as

$$F_N = 2\pi\bar{r}\bar{D}_p\sigma_N/\sqrt{3} \quad (20)$$

$$F_\theta = 2\pi\sigma_\theta A/N \quad (21)$$

$$F_p = 2\pi\bar{r}\bar{D}_p\tau/\sqrt{3} \quad (22)$$

In Equations 20 and 22, \bar{r} is the average radial coordinate of the two nodes forming the bond, and D_p is the perpendicular distance given in Equation 9. In Equation 21, $A = \sqrt{3}(D'_o)^2/2$ is the cross-sectional area of the NABOR node, and N is the number of bonds on the node. This allows a portion of the hoop force to be computed for every bond. This hoop calculation is performed separately for each of the two nodes.

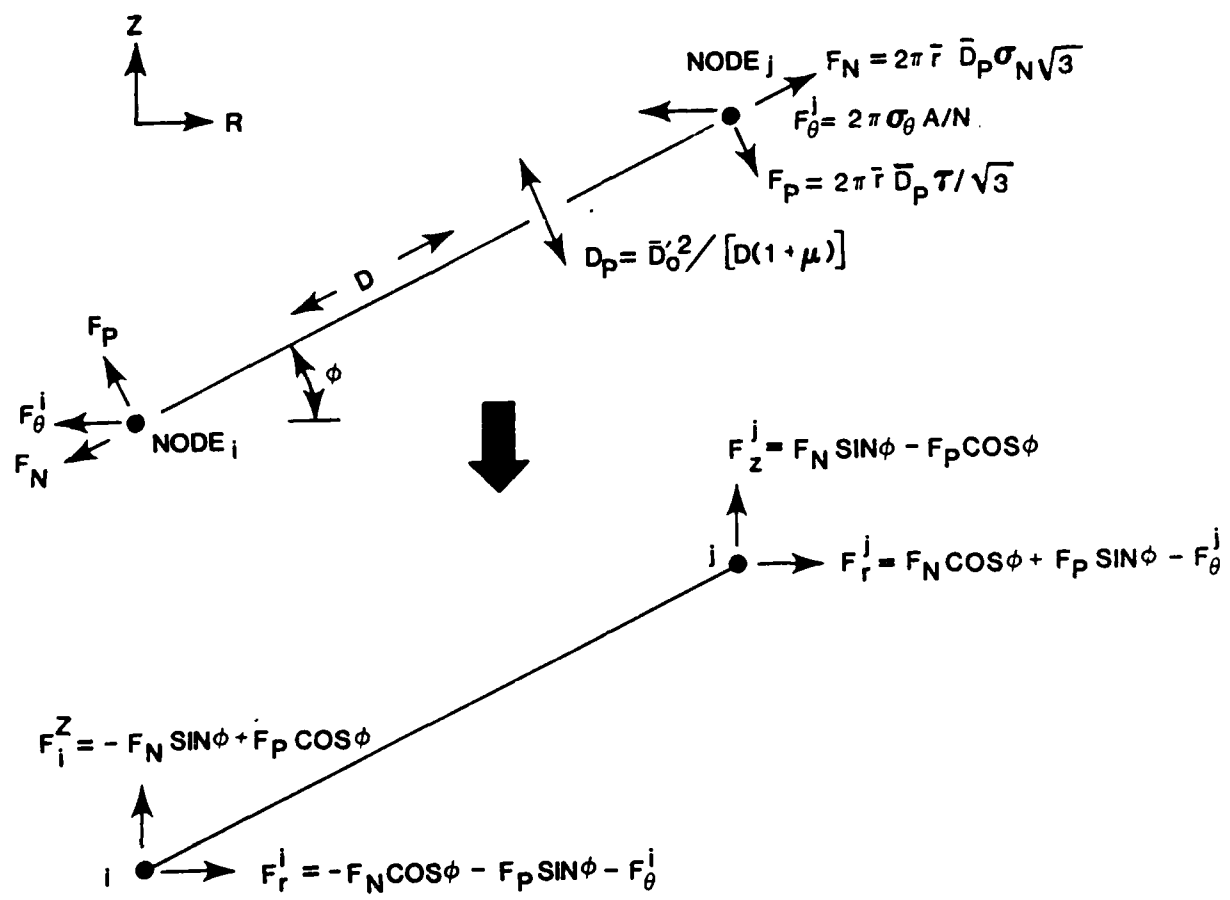


Figure 25. Definition of Nodal Forces for Axisymmetric Geometry

These relationships are derived for a hexagonal close-pack geometry as shown in Figure 26. Unfortunately, for other geometric arrangements, the force-stress relationship is different. For example, a checkerboard arrangement of rows and columns, where there are only four neighbors, gives $F_N = D_p \sigma_N$. Although the work performed to date has used only the relationships of Equations 20-22, it may eventually be preferable to alter these relationships such that they become a function of the current geometric arrangement.

After the normal, hoop, and shear forces (F_N , F_θ , F_p) have been determined, the r and z components (F_r , F_z) are determined as shown in Figure 25. For node i

$$F_r^i = -F_N \cos\phi - F_p \sin\phi - F_\theta \quad (23)$$

$$F_z^i = -F_N \sin\phi + F_p \cos\phi \quad (24)$$

The forces on node j (with the exception of F_θ) are equal and opposite to those on node i . For each specific bond, there is a static moment unbalance of $D \cdot F_p$. These localized unbalances tend to cancel one another and appear to have little affect on the overall system response.

e. Equations of Motion

The nodal equations of motion for node i , the r direction, are

$$\dot{u}_i^{t+} = \dot{u}_i^{t-} + \Sigma F_r^i \bar{\Delta t} / M_i \quad (25)$$

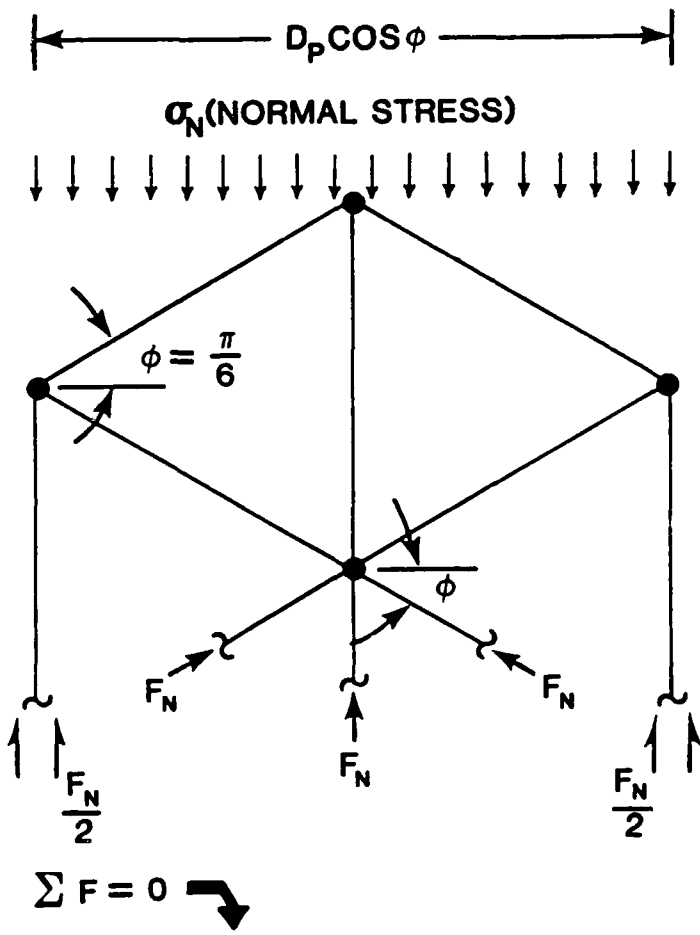
$$r_i^{t+\Delta t} = r_i^t + \dot{u}_i^{t+} \Delta t \quad (26)$$

where \dot{u}_i^{t+} is the constant velocity for the time increment between t and $t + \Delta t$, and \dot{u}_i^{t-} is the velocity prior to time $t = t$. The net force in the r direction is ΣF_r^i , which contains contributions from all bonds containing node i . It can also accept contributions from traditional triangular and/or quad elements, such as demonstrated in Figure 4. The average integration time increment (about time $t = t$) is $\bar{\Delta t}$, and M_i is the mass of node i .

Equation 26 gives the updated nodal positions $r_i^{t+\Delta t}$. The integration time increment, Δt , must be less than the minimum sound speed transit time between any two nodes. The equations of motion in the z direction have the same form as Equations 25 and 26.

f. Searching Algorithm

A schematic of the searching algorithm is shown in Figure 27. The neighbor nodes of NABOR node i are all the nodes within a distance $D \leq 1.3 D_0$ to node i . The neighborhood nodes all have distances $D > 1.3 D_0$, but they are the next closest nodes to NABOR node i . The total number of neighbor nodes plus neighborhood nodes, in this example, is eight. For an interior NABOR node in a hexagonal close pack geometry, there would be six neighbor nodes and two neighborhood nodes.



$$\sum F = 0 \rightarrow$$

$$\sigma_N D_p \cos \phi = 2\left(\frac{F_N}{2}\right) + 2F_N \sin \phi + F_N$$

$$F_N = D_p \sigma_N / \sqrt{3}$$

$$F_N = 2\pi r D_p \sigma_N / \sqrt{3}$$

PLANE STRAIN
(UNIT THICKNESS)

AXISYMMETRIC

Figure 26. Derivation of Force-Stress Relationship for Hexagonal Nodal Arrangement in Axisymmetric Geometry

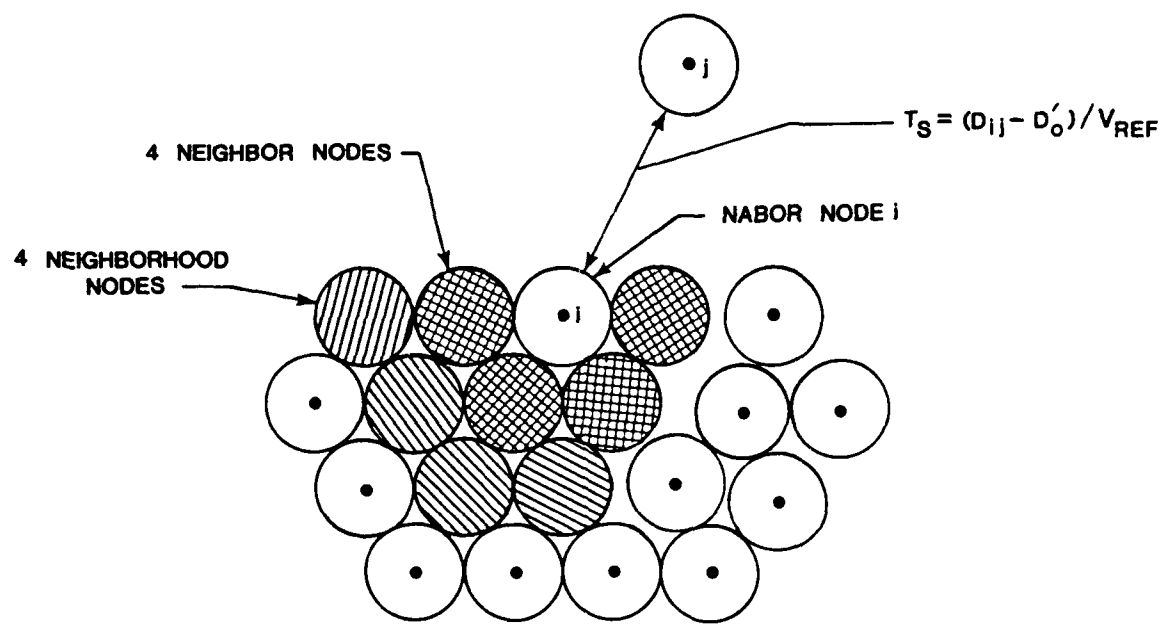


Figure 27. Schematic Representation of the Searching Algorithm

Only the neighbor nodes can affect node i directly by transmitting forces to it. It is helpful to monitor the neighborhood nodes because they are the nodes most likely to become neighbor nodes. The important features of the searching algorithm are as follow.

For every NABOR node, the distances to all neighbor and neighborhood nodes are computed for each cycle of integration. This allows neighborhood nodes to become neighbor nodes as soon as $D \leq 1.3 D'_o$.

Every NABOR node has a timer variable, T_s , which is the minimum time required for a new node (other than a neighbor or neighborhood node) to possibly become a new neighbor. It is expressed as

$$T_s = (D_{ij} - D'_o)/V_{ref} \quad (27)$$

where D_{ij} is the distance between two nodes i and j , and V_{ref} is a reference velocity given by

$$V_{ref} = \max(V_o, \Delta V_{ij}) \quad (28)$$

Here, V_o is a user-supplied input velocity, and ΔV_{ij} is the computed velocity difference (magnitude only) between nodes i and j .

If V_o is larger than any relative closing velocity experienced during the course of the event, then every neighbor node would be found before it gets too close to the associated NABOR node. This may lead to excessive searching, especially for relatively high velocity impact problems.

At the other extreme, if V_o is very small, the V_{ref} will be governed by the computed velocity differences, ΔV_{ij} . This would reduce the searching, and every new neighbor node would probably be found before it gets too close to the associated NABOR node. There may be some instances when the new neighbor nodes would not be found soon enough. When this occurs, it is necessary to restart the computation from an earlier time, using a higher value of V_o . For every cycle of integration, T_s is reduced by Δt .

$$T_s^t + \Delta t = T_s^t - \Delta t \quad (29)$$

When T_s becomes negative, a global search is initiated. This search examines every other NABOR node in the grid and establishes an updated set of neighbor and neighborhood nodes. It also establishes an updated T_s based on distances and relative velocities of all nodes, except the neighbor and neighborhood nodes.

It is at this point that the value of monitoring the neighborhood nodes can be seen. If the neighborhood nodes were not monitored, the T_s would often be governed by one of the neighborhood nodes, and it would often provide a much smaller time until the next search, thus causing more searching.

For a limited number of computations performed to date, the computing time required for searching has not been excessive. It is evident from Equations 27 and 28 that higher impact velocities cause more searching. A counteracting feature is that the time increment does not significantly decrease for the NABOR computations because the minimum distance between nodes is always $D \approx D_o$. For high impact velocities, using traditional Lagrangian techniques, the integration time increment often becomes very small due to the highly distorted grid. This results in more integration cycles (and increased computing time) for the traditional Lagrangian approach.

2. THREE-DIMENSIONAL GEOMETRY

The three-dimensional NABOR algorithm follows the same general approach as the preceding axisymmetric algorithm. In some aspects it is more complicated, due to the third dimension; but in other respects it is less complicated, because all of the hoop-related complications of axisymmetric geometry are eliminated.

This subsection includes a description of the three-dimensional mass distribution, the strains and strain rates, and the concentrated forces. Other portions of the three-dimensional algorithm are very similar to those of the axisymmetric algorithm and will not be repeated. This includes the deviator and shear stresses, the pressure and artificial viscosity, the equations of motion, and the searching algorithm.

The initial NABOR node geometry consists of nested layers of nodes, where each layer has a hexagonal close-pack arrangement, as shown in Figure 28. The projected hexagonal area is $\sqrt{3}D_o^2/2$, and the effective layer thickness is $\sqrt{6}D_o/3$. The resulting NABOR node mass is

$$M = \rho_o D_o^3 / \sqrt{2} \quad (30)$$

Figure 29 shows how the NABOR nodes are attached to the traditional tetrahedral element grid. Here, the layers of nodes are in the x-z plane. This basic grid arrangement was used for the three-dimensional NABOR computation in Figure 12.

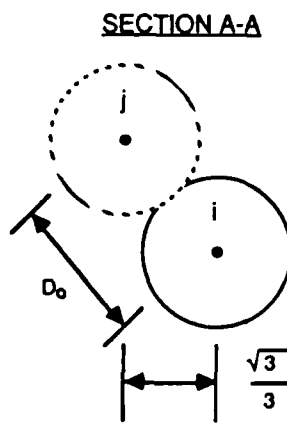
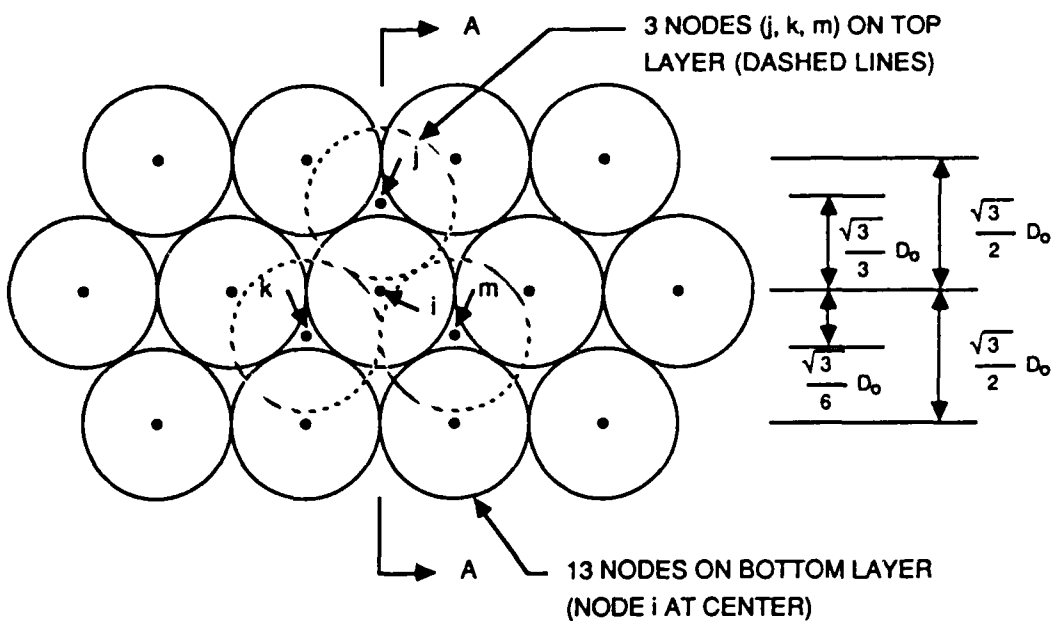
The three dimensional volumetric strains are computed in a manner similar to that used in two dimensions.

$$\mu_1 = D_o/D - 1.2247 \quad (31a)$$

$$\mu_2 = (D_o/\bar{D})^3 - 1 \quad (31b)$$

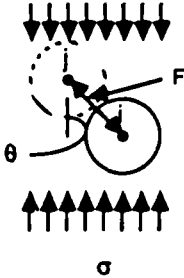
$$\mu = \max(\mu_1, \mu_2) \quad (31c)$$

where D_o is the initial NABOR node diameter, D is the current distance between nodes, and \bar{D} is the average distance of all neighbor nodes that have bonds ($D \leq 1.3D_o$) with the NABOR node. The constant in equation 31a (1.2247) allows pure shear to occur without introducing a significant volumetric strain.



FORCE - STRESS RELATIONSHIP

NORMAL STRESS ON NODE i, σ
TRANSFERRED EQUALLY TO NODES
j, k, m THROUGH THREE FORCES, F.



$$3F\cos \theta = \sigma A$$

$$\frac{\sqrt{6}}{3} = \frac{\sqrt{3}}{2} D^2 \sigma$$

$$F = \frac{\sqrt{2}}{4} D^2 \sigma$$

Figure 28. Arrangement of Three-Dimensional NABOR Nodes

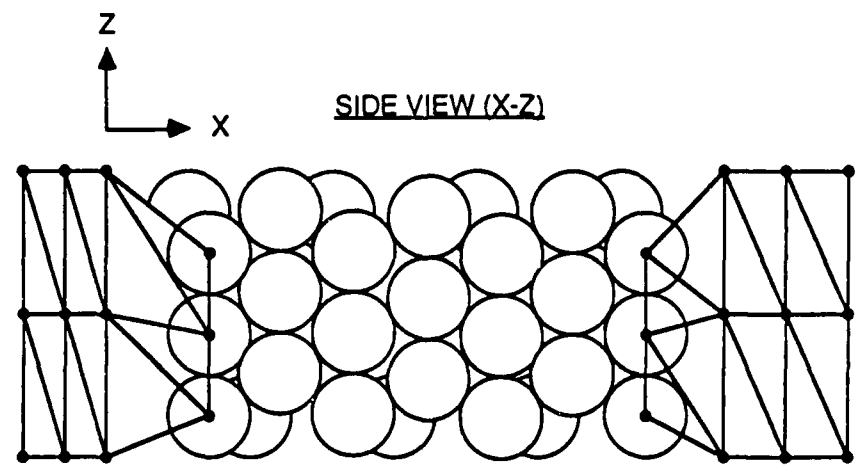
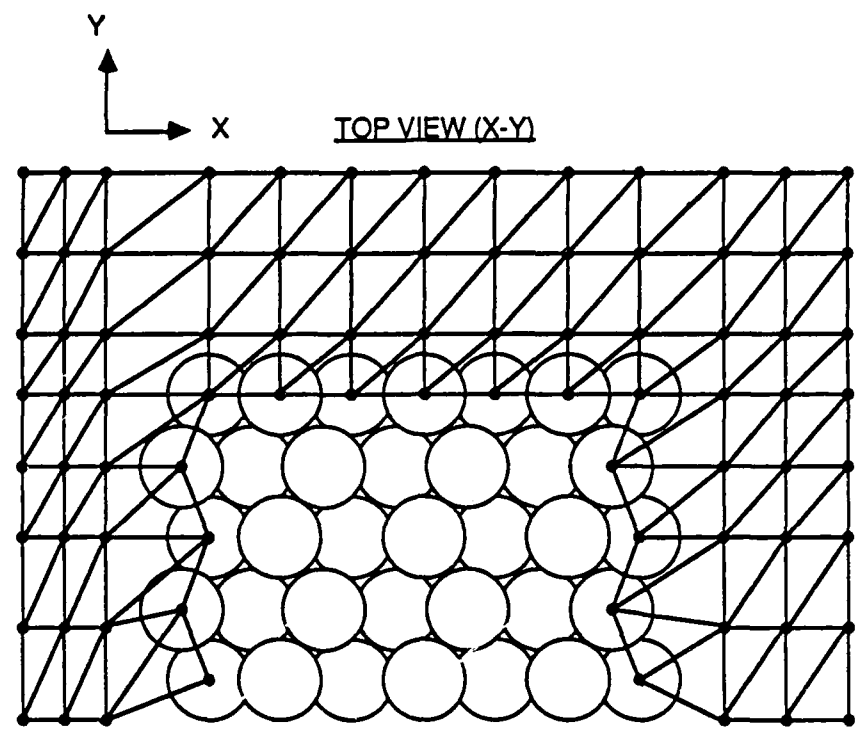


Figure 29. Attachment of Three-Dimensional NABOR Nodes to Traditional Tetrahedral Element Grid

The normal and shear strain rates in three dimensions are similar to the two-dimensional strain rates in Figure 22 and in Equations 2 and 5. The specific formulation for the normal strain rate between nodes i and j is

$$\dot{\epsilon}_N = (A \cdot \Delta V_x + B \cdot \Delta V_y + C \cdot \Delta V_z) / D \quad (32)$$

where A, B, and C are direction cosines from node i to node j, and the velocity differences ($\Delta V_x, \Delta V_y, \Delta V_z$) have the form $\Delta V_x = \dot{u}_j - \dot{u}_i$. The velocities in the x, y, and z directions are designated as \dot{u} , \dot{v} , and \dot{w} , respectively.

There are two additional normal strain rates that are perpendicular to the bond. Because these cannot be determined directly, they are estimated to be

$$\dot{\epsilon}_{P1} = \dot{\epsilon}_{P2} = -0.25\dot{\epsilon}_N \quad (33)$$

This is essentially the same as setting $\beta = -0.5$ in Equation 4.

The net three-dimensional shear strain rate is the net relative velocity (between nodes i and j) that lies in a plane perpendicular to the bond (line connecting the two nodes), divided by the distance between the two nodes. It is expressed as

$$\dot{\gamma} = \sqrt{\dot{\gamma}_x^2 + \dot{\gamma}_y^2 + \dot{\gamma}_z^2} \quad (34)$$

where

$$\dot{\gamma}_x = [(B^2 + C^2)\Delta V_x - A \cdot B \cdot \Delta V_y - A \cdot C \cdot \Delta V_z] / D \quad (35)$$

$$\dot{\gamma}_y = [-A \cdot B \cdot \Delta V_x + (A^2 + C^2)\Delta V_y - B \cdot C \cdot \Delta V_z] / D \quad (36)$$

$$\dot{\gamma}_z = [-A \cdot C \cdot \Delta V_x - B \cdot C \cdot \Delta V_y + (A^2 + B^2)\Delta V_z] / D \quad (37)$$

The equivalent strain rate, $\dot{\epsilon}$, and equivalent strain, ϵ , are as presented previously in Equations 6 and 7.

After the strains and strain rates are defined, the stresses and pressures can be determined in a manner similar to that used in Equations 10-19. The resulting stresses of interest are the total normal stress along the bond, σ_N , and the shear stress, τ .

The lower right portion of Figure 28 shows how the stresses can be converted into forces. The resulting normal and shear forces are expressed as

$$F_N = \sqrt{2} D_p^2 \sigma_N / 4 \quad (38)$$

$$F_s = \sqrt{2} D_p^2 \tau / 4 \quad (39)$$

where $D_p^2 = D^3 / D(1 + \mu)$ tends to adjust the projected cross-sectional area normal to the bond, based on the volumetric strain and the distance between the nodes.

Now, the x, y, and z forces on node i can be obtained.

$$F_x^i = A \cdot F_N + (\dot{\gamma}_x / \dot{\gamma}) F_s \quad (40)$$

$$F_y^i = B \cdot F_N + (\dot{\gamma}_y / \dot{\gamma}) F_s \quad (41)$$

$$F_z^i = C \cdot F_N + (\dot{\gamma}_z / \dot{\gamma}) F_s \quad (42)$$

The forces on node j are equal and opposite to those on node i.

The equations of motion and the searching algorithm are similar to those of the two-dimensional case.

SECTION IV CONCLUSIONS AND RECOMMENDATIONS

This report has presented a series of two- and three-dimensional computations for a steel projectile impacting a concrete target. In two dimensions, it was demonstrated that the eroding target and NABOR target approaches could be used to give results that agreed very well with the more exact tunneling (baseline) approach. In three dimensions, the normal impact conditions were repeated, and although there were some discrepancies, the results are in general agreement with the two-dimensional results. Examples of oblique and yawed impacts were also presented to demonstrate the three-dimensional capability. For these two example problems, there were no significant differences in the monitored equivalent stresses or pressures when compared to the normal impact results.

The axisymmetric and three-dimensional NABOR algorithms have also been presented. The initial results are very encouraging, but more computations must yet be performed to thoroughly assess this technique.

REFERENCES

1. G.R. Johnson and R.A. Stryk, *User Instructions for the EPIC-2 Code*, Honeywell Inc., AFATL-TR-86-51, September 1986.
2. G.R. Johnson and R.A. Stryk, *User Instructions for the EPIC-3 Code*, Honeywell, Inc., AFATL-TR-87-10, May 1987.
3. L. Thigpen "Projectile Penetration of Elastic-Plastic Earth Media," *Journal of the Geotechnical Engineering Division*, ASCE, Vol 100, No. GT3, March 1974.
4. J.J. Osborn and D.A. Matuska, *Hydrocode Analysis of the Impact of a Clustered Airfield Defeat Munition into Concrete*, Eglin Air Force Base, AFATL-DLJW-TN-78-3, February, 1978.
5. K.E. Kimsey, G.H. Jonas, J.A. Zukas and G.R. Johnson, "Computer Solution of a Scaled MK84 Bomb Impact into Concrete," *Proceedings of Sixth International Symposium on Ballistics*, Orlando, FL, October 1981.
6. R.W. Rosinsky "Lagrangian Finite Element Analysis of Penetration Mechanics," *Energy and Technology Review*, Lawrence Livermore National Laboratory, October 1986.
7. G.R. Johnson and W.H. Cook, "A Constitutive Model and Data for Metals Subjected to Large Strains, High Strain Rates and High Temperatures," *Proceedings of Seventh International Symposium on Ballistics*, The Hague, The Netherlands, April 1983.
8. D.A. Matuska, R.E. Durrett and J.J. Osborn, "HULL User Guide for Three Dimensional Linking with EPIC-3," Orlando Technology, Inc., Shalimar, FL, ARBRL-CR-00484, July 1982.
9. G.R. Johnson, R.A. Stryk and J.G. Dodd, "Dynamic Lagrangian Computations for Solids, With Variable Nodal Connectivity for Severe Distortions," *International Journal for Numerical Methods in Engineering*, Vol 23, 1986.
10. B.J. Daly, F.H. Harlow and H.E. Welch, "Numerical Fluid Dynamics Using the Particle and Force Method: Part 1—The Method and its Applications," Los Alamos Scientific Laboratory, LA-3144, April 1965.
11. M.L. Wilkins, "Calculation of Elastic-Plastic Flow," *Methods in Computational Physics*, Vol 3, Edited by B. Alder and S. Fernback, Academic Press, New York, 1964.
12. J.M. Walsh et al., "Shock-Wave Compressions of Twenty-Seven Metals. Equation of State of Metals," *Physical Review*, Vol 108, October 1957.